Edinburgh Research Explorer

Quantifying flow in variably wet microporous carbonates using object-based geological modelling and both lattice-Boltzmann and pore network fluid flow simulations

1 **Quantifying flow in variably wet microporous carbonates using object-based**

2 **geological modelling and both lattice-Boltzmann and pore network fluid flow**

3 **simulations**

4 **Harland. S.R.[1], Wood. R.A.[1], Curtis. A.[1], van Dijke. M.I.J.[2], Stratford. K.[3], Jiang. Z.[2],**

5 **Kallel. W.[2], Sorbie. K.[2]**

6 [1]School of GeoSciences, University of Edinburgh, West Mains Road, Edinburgh, EH9 3JW

7 [2]Institute of Petroleum Engineering, Heriot-Watt University, Riccarton, EH14 4AS

8 [3]EPCC, University of Edinburgh, JCMB, Mayfield Road, Edinburgh, EH9 3JZ

9

16

17 **ABSTRACT**

18 Chalky microporosity can constitute up to 100% of the total porosity within carbonate

19 reservoirs, but its contribution to both single- and multi-phase flow is poorly quantified. We

20 present a flexible, object-based algorithm to construct 3D computational rock

21 representations that reproduce micritic fabrics of chalky microporous carbonates based on

22 calcite crystal fabrics observed in 2D SEM images. By methodologically altering model

23 parameters we begin to explore the state-space of microporous carbonates to quantify

24 single- and multi-phase flow using both lattice-Boltzmann and network flow models.

1

25   Micropore size has little to no effect on single-phase permeability, while differences in

26   multi-phase flow properties are observed for microporous fabrics with pores no smaller

27   than $0.50\mu m^3$ suggesting a change in the pore-scale controls on flow. Single-phase

28   permeability increases by an order of magnitude within fabrics of varying total

29   microporosity (18% to 35%), but minimal effect on multi-phase flow is observed. Similarly,

30   multi-phase flow properties are unaltered by micrite rounding due to burial dissolution,

31   suggesting no alteration in pore-network topology. Micrite rounding, however, notably

32   increases porosity and single-phase permeability in comparison to original rhombic micrite

33   fabrics. The presence of moldic mesopores impacts flow but only when there is a direct

34   connection between them. Otherwise, single-phase permeability is controlled by

35   micropores. Importantly, recovery is dependent on wetting scenario and pore-network

36   homogeneity. Under water-wet imbibition, an increase in pore homogeneity (more

37   micropores) yields a lower residual oil saturation. Together, these results quantify the

38   importance of microporosity in contributing to, or controlling, overall flow and sweep

39   characteristics in carbonate reservoirs.

40   **1. Introduction**

41   Understanding the pore system and petrophysical properties of subsurface reservoir rocks

42   is vital for accurate prediction of fluid flow behaviour and therefore hydrocarbon recovery.

43   Predicting such properties for carbonate rocks can be a particularly complex task as their

44   pore systems are inherently multi-scale, often spanning four relevant orders of magnitude

45   of pore size variation (Choquette and Pray, 1970). Perhaps the least understood type of

46   porosity within carbonates is microporosity. There are many definitions of the class of

47   microporosity, including pores <10µm in diameter and hence below the resolution of an

48   optical microscope (Cantrell and Hagerty, 1999), or pores less than 62.5µm in diameter

49   (Choquette and Pray, 1970), or pores less than 1µm in diameter in at least one direction

50   (Pittman, 1971).

51 Microporosity has many origins, but the most pervasive form of microporosity is known as

52 'chalky' microporosity (Pittman, 1979; Moshier, 1989a; Budd, 1989). Chalky microporosity

53 is formed between the crystal faces of rhombic micrite (micro-crystalline calcite, Figure 1a;

54 see Folk, 1962) which is thought to form through the transformation of acicular high-

55 magnesium calcite and aragonite lime mud crystals into micro-rhombic low-magnesium

56 calcite (Lucia and Loucks, 2013). This occurs via dissolution and recrystallization, although

57 the exact details of the process are still debated (Dravis, 1989; Cantrell and Hagerty, 1999;

58 Heasley et al., 2000; Lambert et al. 2006, Lucia and Loucks, 2013). These pores have a

59 distinct 'plate-like' morphology (Cantrell & Hagerty, 1999) and one spatial dimension

60 maybe up to an order of magnitude smaller than the other two dimensions (Figure 1b,

61 inset) where in the smallest dimension the pores are 0.1μm while in the other two

62 dimension they are around 1μm. Nevertheless, such pores may constitute a significant

63 percentage of the total porosity and of the potential storage capacity (up to 100% in mud

64 dominated facies) of some of the largest known carbonate reservoirs, for example the

65 Middle Eastern Upper Jurassic Arab Formation (Cantrell & Hagerty, 1999; Lambert et al.,

66 2006) and the Lower Cretaceous Thamama group (Moshier, 1989b; Budd, 1989; Smith et

67 al., 2003; Lambert et al., 2006; Cox et al., 2010; Deville de Periere, 2011).

68 Relatively few studies have attempted to quantify the contribution of microporosity to both

69 single- and multi-phase flow. Consequently the resultant effects on petrophysical

70 properties are neither routinely acknowledged or accounted for when assessing reservoir

71 quality. For example, it is commonly assumed that hydrocarbons are unlikely to be

72 emplaced into micropores during primary drainage (due to the small throat diameters,

73 typically <1μm, and resultant high capillary), and that microporosity therefore contributes

74 very little to fluid flow through the reservoir unit, containing only bound, irreducible waters

75 (Pittman, 1971; Kirkham et al., 1996; Cantrell and Hagerty, 1999). Recently, however, the

76 potential importance of micropores has been highlighted by several authors who have

77 shown that it is possible for hydrocarbons to be contained within micropores, especially

78 towards the top of the oil column (Cantrell & Hagerty, 1999; Lambert et al., 2006). Studies

79 have also shown that micropores can influence fluid flow by either decreasing residual oil

80 saturation (Wu et al., 2008; Hollis et al., 2011; Fullmer et al., 2014) or by providing the

81 permeable pathway between otherwise disconnected, larger scale pores (Roth et al.,

82 2011). While micropore-dominated carbonates have low permeabilities (less than 10mD),

83 the pervasive distribution of microporosity has been shown to result in a higher sweep

84 efficiency within intervals with a high percentage of micropores (Wu et al., 2008; Hollis,

85 2011; Fullmer et al., 2014). Additionally, within some multiscale pore networks, micropores

86 provide the connectivity and fluid pathway between larger scales of porosity (Figure 1b).

87 For example, Roth et al. (2011) demonstrated that connectivity through a multi-scale

88 carbonate pore network was only achieved when pores <12µm in diameter were present in

89 the model; in these models, the microporosity actually controlled the percolation threshold.

90 Hence, it is important that the contribution of chalky microporosity to flow is understood

91 and quantified in order for accurate reservoir property predictions to be made.

92 Chalky microporous carbonates have many different fabric properties which can vary

93 throughout a reservoir, and micropore morphology (size and shape) is controlled by the

94 different styles of packing and size distribution of the micrite crystals (Lambert, 2006;

95 Volery, 2010; Deville de Periere, 2011; Fullmer et al., 2014). Microporosity can be found,

96 for example, within micritised grains, or as pervasive horizons of micritic matrix (with or

97 without larger mesopores), or between grains where the inter-granular pore space has

98 been micritised (Cantrell and Hagerty, 1999). An additional feature of some microporous

99 carbonates, particularly those in the Middle East, is micritic dissolution (Budd, 1989;

100 Moshier, 1989b; Wagner, 1990) which is typically found towards the top of the oil column

101 (Lambert et al., 2006). Acidic fluids flowing through the micropore network prior to

102 hydrocarbon emplacement, dissolve the edges and vertices of the rhombic micrite crystals

103 to leave rounded crystals (Figure 1c) with a reduced crystal size (Lambert, 2006).

104 Microporous horizons with rounded crystals due to micritic dissolution have been shown to

105 have better reservoir qualities (high porosity and single-phase permeability) than their

106 rhombic counterparts, and have between 8% and 13% more porosity (Lambert, 2006).

107 However, the effect of micritic dissolution on multi-phase flow properties is unknown.

108 These observations suggest that further research is required on variations in microporous

109 fabric properties and the effects that they have on flow, both individually and in

110 combination. As such, building a flexible computational algorithm to produce digital rock

111 models that incorporate the textural variations of microporous carbonates provides a

112 useful methodology.

113 To understand the flow properties of chalky microporosity, 3D images from computer

114 tomography (XMT) scanners (Van Geet et al., 2000) would be ideal. Chalky microporosity,

115 however, is below the resolution of standard micro-computer tomography (μ-CT) scanners,

116 and although nano-CT scanners (resolution $<100nm^3$/voxel) are capable of imaging

117 microporosity, the sample volumes ($<15\mu m^3$) are too small to acquire a statistically

118 significant dataset. Direct 3D images also provide very little flexibility to study the effect on

119 flow of variations in microporosity as the properties of the rock fabric in the image cannot

120 be adjusted with ease, if at all. As such, rock reconstruction methods that focus on

121 reproducing geological fabrics to infer the pore-space, provide a more viable and flexible

122 methodology. Indeed, the pore network of a rock is created by its fabric, so by accurately

123 reconstructing the solid phase(s), the pore network and therefore the petrophysical flow

124 characteristics (e.g., porosity, absolute permeability, relative permeability and capillary

125 pressure curves) of the medium can be determined.

126 Many different methodologies have been developed to produce 3D models of porous

127 media. For example, there are object-based modelling methods including process-based

reconstructions (Bakke and Øren, 1997; Øren and Bakke, 2003) and continuum based reconstructions (Biswal et al. 2007; 2009a,b) and there are statistical or stochastic reconstructions from 2D images (Okabe and Blunt, 2004; Al-Kharusi and Blunt, 2008; Wu et al., 2004, 2006; 2008).

While all proposed methods provide advantages for certain applications, they have limitations for modelling microporosity. For example, reconstructions based on the spatial statistics of 2D images can be used to create 3D models using multipoint-statistic techniques (Okabe and Blunt, 2004; Al-Kharusi and Blunt, 2008) or stochastic approaches involving Markov meshes (Wu et al., 2004, 2006; 2008). These statistical approaches, however, tend to smooth the true variations in the image structure, and as such fail to capture the heterogeneous nature of multiscale pore systems such as those within carbonates. Object-based models provide perhaps the most flexible basis for modelling rock fabrics as the fabrics can be altered and adjusted to recreate all geological variability based on observations. However, the complex processes of carbonate diagenesis mean that process-based modelling methodologies, which work very well for reconstructing sandstones (Bakke and Øren, 1997; Øren and Bakke, 2003), are problematic to implement for carbonates. For an application of the method to chalky microporosity in particular, the diagenetic process of formation of micrite is not only poorly understood, but may also vary from reservoir to reservoir (Budd, 1989; Moshier, 1989a; Moshier, 1989b; Cantrell and Hagerty, 1999; Lambert et al., 2006; Richard et al., 2007; Volery et al., 2009; Lucia and Loucks, 2013). While continuum based modelling methodologies (e.g. Biswal et al. 2007; 2009a,b) provide a unique approach which combines low resolution micro-CT scans with 2D geological/crystal information in a continuum object-based technique to reproduce carbonate fabrics at multiple resolutions, such an approach did not produce models with a resolution high enough to examine microporosity, limiting quantification of the effect of microporosity on the petrophysical flow properties of the rocks in question (Roth et al.,

154   2011).

155   In this study, we present an object-based digital rock building methodology that aims to

156   accurately reconstruct the fabric of chalky microporous carbonates in order to accurately

157   capture relevant statistical properties of the pore space. Both quantitative and qualitative

158   underlying data are used to populate the models based on data from 2D SEM image

159   analysis. The algorithm is flexible such that it can model the textural variations of

160   microporous carbonates and include multiple scales of porosity. This new methodology is

161   thus able to reconstruct reservoir rocks at a resolution capable of capturing microporosity,

162   enabling interrogation of both single-phase and multi-phase flow in chalky microporous

163   carbonates.

164   In what follows, we use the algorithm in combination with a lattice-Boltzmann simulator, a

165   network extraction algorithm and a multi-phase phase flow simulator to study the single-

166   and multi-phase flow properties of synthetically generated typical Middle Eastern chalky

167   microporous carbonates. In particular, we consider the effect of micropore size, total

168   micropore content and the effect of micritic dissolution within models of purely micritic

169   matrix. Finally, we examine how moldic mesoporosity within a microporous network affects

170   the flow properties of synthetically generated multiscale pore networks.

171   **2. METHODOLOGY**

172   **2.1.   Textural Properties of Micrite and Micropores**

173   The 3D model needs to be calibrated with geostatistical data. Since it is not possible to

174   image chalky microporosity directly using 3D scanning methods, following other studies

175   (Biswal et al., 2007, 2009a, 2009b; Deville de Periere et al., 2011) we use scanning

176   electron microscope (SEM) images to capture the basic textural properties of microporous

177   carbonates. Image analysis is performed using IMAGEJ (Schneider et al., 2012).

178   Different types of SEM images are used to extract both quantitative and qualitative data to

calibrate the models. Secondary electron images (Figure 1) provide a shallow, pseudo 3D image of rough cut chips which allows the crystal form and the nature of the contact between crystals to be examined. For example, the micrite in the chalky microporosity sample in Figure 1a consists of approximately equidimensional euhedral rhomboids, often with multiple facets, and there is no obvious alignment of crystal orientation.

Images of epoxy resin pore casts (Figure 1b) are used provide insight into the form, size and distribution of different pore types (macropore and micropore) within a sample. They also provide crucial information about the nature of 3D connectivity between pores. For example, the highly connected sponge-like network of platy microporosity, and the connectivity between this network and a mesopore, can be seen in Figure 1b.

Finally, backscatter images of highly polished, flat sample surfaces (Figure 2a,b) provide a good contrast between pore and solid. They enable easy binarisation to determine 2D slice porosities and also allow measurements of crystal diameter to be made within the image plane. SEM images are taken at a very high resolution (here up to 0.10μm/pixel) and as such, before any crystal diameter data are extracted through image analysis, the resolution of the SEM image needs to be reduced (by averaging across neighbouring pixels) to match that of the models which will be built. This removes features that would be unresolvable at the model resolution.

After binarisation and resolution reduction, a watershed algorithm can be applied to detect individual crystals and Feret diameter measurements (with amalgamated crystals removed) can be made to provide a quantitative crystal size distribution (Figure 2c) from which the model can be populated. Where it is not possible to detect crystal edges through an automated process, manual measurements of the longest diagonal length of the crystal can be made instead. The resulting data are 2D crystal diameters. By collecting a statistically significant number of diameters (here, over 400 measurements) these are

204   assumed to be reflective to the 3D crystal diameters.

205   **2.2   Object-Based Reconstruction Methodology**

206   The crystal size distribution (Figure 2c) is used to build a library of 3D micrite crystals at

207   the desired resolution, including forms rotated around the x, y and z axes at discrete

208   intervals throughout the desired range of rotations. Micrite crystals have multiple facets

209   and so a very high resolution digital model would be required to capture the crystal facets

210   correctly. As such the rhombs are simplified to cubes; this maintains the approximately

211   equidimensional and euhedral nature of micrite, but reduces the voxel resolution required

212   to represent the crystal form. The algorithm is flexible such that if multiple crystal types,

213   shapes and sizes were required, these could simply be included in the library.

214   When distributing the crystals, matrix connectivity is guaranteed by allowing (or forcing) an

215   overlap of neighbouring crystals. Crystals in the library have a layered structure where

216   voxels on the edges of the crystal are identified; these are allowed to overlap with other

217   crystal edge voxels, while crystal centres must remain non-overlapping (Figure 3a, b). This

218   technique has similarities to the 'cherry-pit' or penetrable-concentric-shell (PCS) model

219   (Torquato 1984, 1985, 1986). As such, the smallest crystal size for any model resolution is

220   3^3 voxels to ensure both a distinct crystal centre and edge voxels (Figure 3c, d). The

221   degree of overlap can be varied so as to suitably represent different micritic textures

222   observed in samples. This allows different styles of micrite packing to be represented, but

223   a minimum edge layer thickness of one voxel is required at any resolution, to maintain

224   matrix connectivity.

225   The rock reconstruction is initialised within a 3D space, discretised into a grid of regular

226   cubic voxels of a predefined physical size (the resolution). In an iterative process, voxels

227   are defined as solid by randomly fitting micrite crystals from the library into the grid. This

228   continues until a desired total percentage of solid, and therefore the desired total porosity

229 (ϕ_D) is achieved. Crystals are fitted from largest to smallest, with the number of iterations

230 (N_i^C) of each crystal size (indexed by i) calculated based on the known crystal frequency

231 distribution (f_i^C, as shown for example in Figure 2c), the volume of each crystal size (V_i^C),

232 the total volume of the grid being filled (V), and the total porosity (ϕ) required in the final

233 model which is related to ϕ_D as described below. As such the number of iterations of each

234 crystal size required to achieve the target porosity is predetermined based on the ratio (R)

235 between the volume of solid produced by the crystal size distribution and the volume of the

236 model to be created as shown in Equations (1) and (2):

237 $$R = \frac{V}{(1-\phi) \times \sum_{i=1}^{n} V_i^C \times f_i^C} \qquad (1)$$

$$N_i^C = R \times f_i^C \qquad (2)$$

238 The overlapping edge voxels of the crystals result in an underestimate of the number of

239 crystals required to fill the volume as overlapping edges are not accounted for in Equations

240 (1) and (2), hence the resulting final porosity would always be higher than the required

241 porosity. To account for this, the target porosity (ϕ in Equations (1) and (2)) is set at a

242 value that is predictably lower than the desired porosity (ϕ_D). This prediction is based upon

243 a sensitivity test to determine the average loss in solid voxels due to overlap at a desired

244 porosity. An example is shown in Figure 4.

245 At each iteration, a random (possibly rotated) crystal of the correct dimensions is selected

246 from the crystal library, and randomly selected potential grid locations are successively

247 tested until a location that satisfies the edge and centre placement conditions is found.

248 Upon completion, the algorithm results in a binary model (Figure 3b) of the foreordained

249 porosity (ϕ_D) that is 100% microporosity and a solid proportion that is 100% micrite.

250 Information specific to each crystal placed into the model such as crystal centre

251 coordinates, crystal diameter and rotational information, is stored in an array as objects

252 are placed into the volume. This information may be used to manipulate the model fabrics

253 to perform rounding of the micrite crystals to emulate micritic dissolution, or to include

254 larger scale features such as mesoscale porosity (pores >10μm in diameter) and cements.

255 The properties of mesopores and cements can be determined from the SEM images in a

256 similar manner to the properties of micrite.

257 Micrite rounding is performed homogeneously across the model volume. The cubic form of

258 the micrite crystals is altered to a spherical form by tracing the inscribed radius of the

259 crystals based on their diameter. Because of the alteration to the fabric it is again

260 important to ensure matrix connectivity of the rounded crystals. This is achieved by testing

261 that each crystal touches at least one other. If this is not satisfied, slight shifts of the

262 unconnected crystals are made to abut them against another crystal. In the highest

263 porosity models generated for this study, this shift process affected less 0.4% of the

264 crystals, but must nevertheless be performed to reflect the rock texture and avoid floating

265 crystals in the matrix.

266 The purely microporous models can subsequently be merged, under certain conditions,

267 with larger scale pores to generate multiscale networks. The mesopore networks can be

268 derived from subsections of micro-CT images or can be synthetically generated to

269 represent, for example, moldic mesopores. Moldic mesopores occur through the

270 preferential dissolution of forams during burial and an example of such is a mould is shown

271 in Figure 1b. The modelled moldic mesopores here are simplified to spherical bodies,

272 although more complex shapes can be used. The size and location of the moulds within

273 the modelled volume can be determined randomly or predefined.

274 Although this process of merging the two pore systems does not reflect the processes of

275 formation of the mesopores and the micritic matrix, the fabrics generated do reflect those

276 observed from SEM analysis such as the connectivity between mesopores and

11

microporosity (Figure 1b) and the rugosity around mesopore edges due to micrite crystals (Figure 2b). The micrite crystals that exist around the edges of the mesopores can also be used as nucleation sites for pore-occluding cements such as those seen in Figure 2b, but we do not study that aspect of the pore system in this paper.

2.3   Sensitivity Analysis of Fluid Flow Properties to Rock Fabric Properties

Here in we explore the variability of chalky microporous carbonate rocks to investigate the flow properties of the different fabrics. First, we investigate the sensitivity of flow properties to micropore size, controlled by varying the resolution at which each model is generated. The size of micropores is likely to vary from reservoir to reservoir and also within any individual reservoir. Models were generated at five different resolutions: $0.50\mu m^3$/voxel, $0.40\mu m^3$/voxel, $0.30\mu m^3$/voxel, $0.20\mu m^3$/voxel and $0.10\mu m^3$/voxel, with three realisations generated at each resolution. Each resolution model had a porosity of approximately 26% and a volume of 400^3voxels and therefore the physical volume size varied between models (Table 1). Both single- and multi-phase flow were simulated on the full 400^3voxel volume models; however in order to be able to compare the properties of the different fabrics properly, eight subvolumes of the four lowest resolution models were also isolated. These subvolumes each had the same physical volume as the highest resolution model ($0.10\mu m^3$/voxel) which had a volume of $40^3\mu m^3$. The voxel sizes of these subvolume models are shown in Table 1.

Secondly, we consider the effect on fluid flow of total porosity within a purely micritic (and therefore purely microporous) fabric and also investigate the effect of micritic dissolution on flow for varying total porosity. Within a microporous reservoir, the total microporosity within micritic matrix varies (Fullmer et al., 2014) and models of varying total matrix porosity were generated to interrogate the single-phase and multi-phase flow properties of 100% microporous fabrics. Total porosity was varied from 18% to 35% and three

302 realisations of each model were created. These porosities are within the range of reported

303 values for purely microporous carbonates (Volery et al., 2010; Deville de Periere et al.,

304 2011; Fullmer et al., 2014) and of porosities from SEM image analysis performed for this

305 study. These models were created at a resolution of 0.40µm^3/voxel and were 400 voxels

306 (or 160µm) in length. Here we also examine the effect of micritic dissolution on flow

307 properties by performing micrite rounding on one model at each given porosity.

308 Finally, we investigate the effect of the presence of synthetic spherical moldic mesopores

309 within a micritic matrix of varying total (micro- and meso-) porosity. Although fully

310 microporous horizons do exist within reservoirs, it is additionally important to understand

311 the range of multi-scale fabrics in which micropores do (and do not) contribute to flow. A

312 mesopore was placed in each octant of a 400voxel^3 model generated at 0.40µm^3/voxel

313 resolution. Amongst other properties, the size of forams varies and as such, the radii of the

314 mesopores in the grid were varied between 10µm and 45µm, generating five different

315 mesopore models. These mesopore models were combined with purely micritic matrices,

316 with microporosities of 18%, 25% and 35%.

317 All models generated during this study were populated with crystals from the crystal size

318 distribution extracted from SEM image analysis of samples (Figure 2c), discretised to the

319 correct resolution in each of the above cases in order to create appropriate corresponding

320 crystal libraries.

321 **2.4   Simulation of flow**

322 Two separate methodologies are employed to simulate single- and multi-phase flow in this

323 paper. We describe each in turn.

324 **2.4.1. Single-phase Flow Simulation**

325 Single-phase flow simulation for the computation of absolute permeability is performed

326 directly on the discretised model using a multiple relaxation time (MRT: Chun and Ladd,

327   2007) lattice-Boltzmann model (Ludwig: Desplat et al., 2001) which represents the

328   boundaries of solid objects using a simple bounce-back scheme. Simulations are

329   performed in lattice units (lu), and converted to SI units (mD) based on the true voxel size

330   (Δx). A permeability is obtained by computing the steady-state volume flux in a periodic

331   system (obtained by reflecting the volume along the flow direction and using periodic

332   boundaries) generated by a constant body force with a viscosity (η) of 1/6 in all cases. The

333   simulations were parallelised and used 2048 cores on the Blue Gene/Q supercomputer

334   based at the Edinburgh Parallel Computing Centre.

335   The steady state volume flux (Q) is related to the macro-scale permeability (k) by the

336   Darcy equation (Equation (3) below, Darcy, 1856) where the differential pressure ($P_b - P_a$)

337   is related to the applied body force and the length of the system in the flow direction (L) of

338   cross-sectional area (A) by

$$Q = -\frac{kA}{\eta}\frac{(P_b - P_a)}{L}$$
(3)

339   As is usual with this type of calculation, we ensure that the final pore-scale Reynolds

340   number is below unity to simulate incompressible Newtonian, laminar flow. For the

341   narrowest pores in the system, we would expect the flow to be poorly resolved which

342   would lead to some systematic, and likely, underestimates in the permeability. Tests in

343   capillaries with regular geometries (circular, triangular, square cross-section) suggest

344   errors in computed permeability to be up to ≈25% for widths less than ~4Δx (Sengupta et

345   al. 2012).

346   **2.4.2. Multi-phase Flow Simulation**

347   We perform multi-phase flow simulations on pore networks extracted from the generated

348   models using the Pore Architecture Tool (PAT) algorithm developed by Jiang et al. (2007).

349   This method is based on extracting the local medial axis through the pore space (using a

350   thinning algorithm) and separating the network into pore bodies and throats (nodes and

351 bonds), preserving the connectivity and topological characteristics of the pore space.

352 Junctions in the network are defined as pore bodies (nodes) and the connecting pathways

353 between nodes are then throats (bonds). Quantitative geometrical characteristics of the

354 network elements such as pore radius, perimeter and area, shape factor and coordination

355 number (the number of bonds connecting to each node in the network), are all determined.

356 These geometrical properties control the development and stability of wetting layers within

357 the network elements (Blunt, 1998; Valvatne and Blunt, 2004). The topology (or

358 connectivity) of the network plays an important role in controlling the multi-phase flow of a

359 network and this can be described for the extracted pore network by calculating the

360 specific Euler number (χ, Vogel and Roth, 2001) which is simply the number of nodes (N)

361 minus the number of bonds (B) divided by the volume of the model (V):

$$\chi = \frac{N-B}{V} \qquad\qquad\qquad\qquad (4)$$

362 The Euler number can also be used to derive the pore size dependent connectivity

363 function by removing pores from the network in order of increasing size and recalculating

364 the Euler number at each step (Vogel and Roth, 2001). Removing larger and larger pores

365 will eventually result in a positive Euler number (fewer bonds than nodes) which indicates

366 the point at which the network becomes unconnected and as such an Euler number of

367 zero is a proxy for the percolation radius of the network.

368 Multi-phase flow was simulated on the extracted networks using the quasi-static (capillary

369 dominated flow) Poreflow software (Valvatne and Blunt, 2004) where two-phase flow is

370 simulated according to invasion-percolation principles during drainage (invasion of oil) and

371 imbibition (invasion of water). A pressure gradient is applied to each phase across the pore

372 network (between the inlet and outlet face) and the relative permeabilities of each phase

373 are determined by calculating the pressure distribution in response to the change in

374 pressure gradient across each phase, using mass conservation, at each node (Øren et al.,

375   1998).

376   In order to simulate multi-phase flow, the pore-scale wetting properties of the model must

377   be predefined. However, the wetting properties of carbonates and microporosity are poorly

378   understood. Strong variations of wettability in different reservoirs are observed more

379   frequently in carbonate reservoirs than in siliciclastic reservoirs (Bobek et al., 1958) and

380   studies into the wettability of globally distributed carbonates (e.g. Treiber and Owens,

381   1972; Kashfi, 1974; Morrow, 1976; Chillingar and Yen, 1983; Cuiec, 1984) have indeed

382   produced varying results. But at the core plug scale, most carbonates have been found to

383   have an intermediate wetting state (Skauge et al. 2006), i.e. they have a weak affinity

384   towards oil. Estimating wettability at the core plug scale is a complex task in itself and few

385   studies have been able to examine the wettability distribution at the pore scale. Here, two

386   different imbibition (water flood) wettability scenarios at the pore scale were simulated to

387   characterise concomitant variations in the multi-phase flow properties. For both scenarios,

388   the pore network is initially assumed to be strongly water-wet and oil flooding (water

389   drainage) continues until a residual water saturation of 0.02 has been achieved. For the

390   first imbibition scenario, the rock remains water wet after drainage and no aging occurs.

391   The second imbibition wettability scenario was performed under a simple fractionally wet

392   scenario where 50% of the pores become oil-wet after drainage (due to aging). This type

393   of wetting is neither pore shape nor pore size dependent, and the oil wet-network elements

394   are randomly distributed throughout the network. Imbibition continues until a minimum

395   residual oil is achieved.

396   **3. Results**

397   **3.1   Effect of Micropore Size**

398   **3.1.1.   Model Fabric Properties**

16

399 As can be seen from Figure 5, the morphology of the micritic fabric in the model matches

400 well with that which is observed in the SEM image.

401 Figure 6 shows 2D slices through a 3D realisation at each resolution, scaled relative to

402 their physical sizes. Visually the models can be seen to be producing very similar micritic

403 fabrics, the simple difference being that the pores and crystal are represented by an ever

404 increasing number of voxels as resolution is increased from $0.50\mu m^3$/voxel up to

405 $0.10\mu m^3$/voxel (a to e respectively in Figure 6), and the size of the smallest resolvable

406 feature decreases with each increase in resolution.

407 ### 3.1.2. Pore Network Properties

408 The pore radii distributions shown in Figure 7a indicate the change in pore geometry with

409 model resolution. The box in Figure 7a shows the smallest pores in the generated models

410 and these pores are equal to the resolution of the model (half a voxel in radius). As the

411 resolution is decreased progressively from 0.10 to 0.50 μm^3/voxel, the smallest pores are

412 lost from the volumes and (at the other end of the scale) larger pores are incorporated.

413 This is reflected in the increase in the average pore radius with a decrease in resolution

414 (Table 2) and an increase in the upper limit of the pores captured by the models (Figure

415 7a).

416 The percolation radius (where the Euler number is 0) can be seen to be dependent on

417 model resolution. The models generated at $0.10\text{-}0.40\mu m^3$/voxel have a percolation radius

418 of ~0.3µm while the model at $0.50\mu m^3$/voxel shows a distinct increase to a percolation

419 radius of 0.38µm. At a resolution of $0.50\mu m^3$/voxel the smallest connections (which control

420 flow in the models of higher resolution) have been lost, and as such the geometry and

421 topology of the system has been altered changing the connectivity of the pores. This

422 change in network properties is highlighted by the decrease in the number of nodes and

423 bonds from $0.40\text{-}0.50\mu m^3$/voxel (Table 2). A change in the fluid flow properties of the

424    $0.50\mu m^3$/voxel model in comparison to the other resolution models could be expected.

3.1.3.   Porosity and Single-phase Permeability

426   All models had a target porosity of 26% and at each resolution a separate target porosity

427   trend (Figure 4a) had to be generated. The resultant model porosities fluctuate randomly

428   around 26% porosity, ranging from 26.8% porosity for the $0.10\mu m^3$/voxel model down to

429   25.9% porosity for the $0.40\mu m^3$/voxel model (Figure 8a). The model subvolumes (Table 1)

430   also show a narrow range of porosities indicating that a reasonably homogeneous medium

431   and representative elemental volume is being generated at all resolutions. The number of

432   crystals generated in each full size model is shown in Table 2.

433   Single-phase permeability (Figure 8b) shows limited variability across all models (between

434   1.8mD and 2.8mD), including for the $0.50\mu m^3$/voxel model which displays no distinct

435   increase in permeability in comparison to the other resolutions. Additionally, there appears

436   to be a negative correlation between porosity and permeability due to changes in

437   resolution (Figure 8c); however over the range of porosities and permeabilities shown, the

438   variation in permeability is <1mD and in porosity is (<1.5%).

3.1.4.   Multi-phase Flow

440   Figure 9 shows the relative permeability curves from the multi-phase flow simulations over

441   the full 400^3voxel models at each resolution. These plots indicate the effective permeability

442   of the water and oil phases against saturation. The relative permeability curves of all

443   models are smooth indicating a homogeneous pore network at all resolutions.

444   The drainage curves for all models are similar (Figure 9a). Resolution (or average pore

445   size) can be seen to have little to no effect on water relative permeability, except for the

446    $0.50\mu m^3$/voxel resolution model which behaves slightly differently at mid-range saturations,

447   possibly reflecting the different connectivity and pore size distribution present. There is a

448   trend of decreasing oil relative permeability at the same saturation with a decrease in

449 resolution.

450 However, upon imbibition the models exhibit separate behaviour depending on their

451 resolution. For both wettability scenarios, the relative permeability curves for models of

452 resolution 0.10-0.40µm^3/voxel are indistinguishable while the relative permeability curves

453 of the 0.50µm^3/voxel models behave slightly differently. This is most pronounced for the

454 water relative permeabilities (Figure 9b&c) which show a higher relative permeability at the

455 same saturation in comparison to the higher resolution models. These differences in

456 relative permeability result in a residual oil which is dependent on resolution (and therefore

457 average pore size, Table 2) and is most clearly demonstrated by the capillary pressure

458 curves in Figure 10b,c. Under water wet imbibition (Figure 10b), the four higher resolution

459 models show an incremental variation in the residual oil saturation (fractional volume of oil

460 remaining in the model after full water flood), from 38% and 28%, while the residual oil

461 decreases notably more, to 23%, for the 0.50µm^3/voxel resolution model. Similarly,

462 although there is no incremental trend for the higher resolution models, under a fractionally

463 oil wet scenario (Figure 10c) the residual oil decreases substantially from around 24% to

464 15% for the model at 0.50µm^3/voxel resolution.

465 These results tend to suggest that the pore network of models generated at 0.50µm^3/voxel

466 resolution have sufficiently different properties (such as connectivity and pore size range

467 and distribution) such that the multi-phase fluid flow properties of these models is altered

468 in comparison to the higher resolution models.

469   **3.2   Effect of Total Microporosity and Micritic Dissolution**

470   **3.2.1.   Model Fabric Properties**

471 Figure 11 shows 2D slices through a 3D realisation of each porosity model. Visually the

472 average pore size can be seen to increase with porosity, and the models appear to

473 represent a statistically homogeneous medium, with some random clustering of crystals as

474   is observed in SEM images.

475   The fabric of a rhombic micrite crystal model can be seen more clearly in Figure 12a and

476   Figure 12c which show the cubic/rhombic and euhedral micrite structure. Additionally

477   Figure 12 shows the effect of rounding on the crystal fabric. In Figure 12b & Figure 12d the

478   original grain structure is retained but without crystal vertices. Any apparently floating

479   grains are connected in the third dimension. The decrease in crystal size after micrite

480   rounding is demonstrated in Figure 12e.

481   ### 3.2.2.   Pore Network Properties

482   Within the rhombic crystal models, average pore size increases with an increase in

483   porosity (Figure 11) which is supported by the results of the pore network extraction

484   analysis presented in Figure 13a. There is also an increase in the range of pore radii with

485   porosity although the range of pores captured in each model spans only one order of

486   magnitude and the majority of pores in the models have a radius of one voxel (two voxels

487   in diameter, Figure 13a). The homogeneity of the micritic fabric results in a narrow range of

488   pore radii reflecting a fairly homogeneous pore network distribution. The increase in

489   average pore size coincides with an increase in the average coordination number (Table 3)

490   while the total number of elements decreases for the models with the highest porosities.

491   The percolation radius increases with porosity (Figure 13c) which would be expected as

492   the average pore size increases. The 18% to 25% porosity models have a similar

493   percolation radius of 0.25μm, while the 30% and 35% porosity models show an increase to

494   0.35μm and 0.40μm respectively, indicating that larger pores are better connected in the

495   higher porosity models, which is again reflected in the average coordination number (Table

496   3).

497   In comparison to their rhombic crystal counterpart, the rounded micrite models exhibit an

498   increase in the range of pore sizes present and also an increase in the average pore

20

radius (Figure 13b), due to the decrease in crystal size (Figure 12e). Individually comparing a rhombic micrite model to its rounded counterpart demonstrates this trend clearly (Figure 13e).

The percolation radius increases after rounding for all models (Figure 13d & Figure 13f). However the average connection number does not show an increase across all models (Table 3). The increase in average connection number after rounding in comparison to before rounding is most pronounced for the low porosity models and this increase tapers off to become zero for the highest porosity models which exhibit no change in average connection number between the rhombic micrite to the rounded micrite fabrics. After rounding, all models have an average connection number of greater than 4.2.

3.2.3.   Porosity and Single-Phase Permeability

The single-phase permeability and porosity results averaged over the individual results of the three realisations for each rhombic crystal model are shown in Figure 14a&b. For each set of realisations the three permeability values were within 0.01mD of the mean and the porosities were within 0.04% of the mean hence the variance was negligible. Over the range of porosities modelled there is an order of magnitude variation in the single-phase permeability, from 0.6mD to 7.5mD.

The effect of micrite rounding on porosity was slightly more pronounced for the lowest porosity models which exhibit an increase of 8% in porosity compared to a 7% increase for the models with the highest initial porosity (Figure 14b). The increase in porosity with rounding is reflected in the substantial increase in single-phase permeability for each individual model as shown by the dashed lines connecting the rhombic models to their rounded counterparts in (Figure 14b).

3.2.4.   Multi-phase Flow

Based on the pore network properties of the original rhombic crystal models, the increase

524 in the average coordination number with increasing total porosity suggests that there

525 would also be a variation in the multi-phase flow properties for these models. However,

526 this expected trend is not observed (Figure 15a, b and c). During drainage (Figure 15a),

527 the oil relative permeability curves can be seen to depend on model porosity. Increasing

528 the porosity leads to a higher oil relative permeability at the same saturation, most likely

529 due to the presence of larger pores and due to the increase in connectivity with porosity.

530 Water relative permeabilities are however almost indistinguishable, showing only a small

531 variation between models and no discernable trend with porosity. An irreducible water

532 saturation of 0.07 is achieved for all models.

533 The imbibition curves for these models are indistinguishable (Figure 15b and c). There is,

534 however, a distinct difference between the residual oil saturation between the two

535 scenarios as water wet imbibition results in a residual oil saturation of 25% while the

536 fractionally wet scenario results in a residual oil saturation of 40%, which is more apparent

537 in the capillary pressure curves (Figure 16).

538 The results and trends for the rounded micrite models (Figure 15d,e,f) reflect the results of

539 the rhombic crystal model. Oil relative permeability curves during drainage show slightly

540 different behaviours dependent on total porosity whilst the imbibition curves are

541 indistinguishable. Moreover, the trends and curves for the two different crystal fabrics

542 cannot be distinguished from each other and so rounding the micrite crystals appears to

543 have little to no effect on multi-phase flow properties in comparison to the rhombic

544 counterpart.

545 **3.3   Effect of Mesoporosity within a Micritic Matrix**

546 **3.3.1.   Model Fabric Properties**

547 The synthetic moldic mesopores modelled in this study were all located in the centre of

548 each octant within the grid. Therefore, as the mesopore radii are increased, the distance

22

separating the mesopores decreases (Figure 17, Table 4). The only model in which the mesopores touch and create a permeable pathway without microporosity is in the final model (Figure 17f) where mesopores have a radius of 45µm. This model is a purely synthetic, conceptual example to examine the change in behaviour upon introduction of a connected mesopore network. In all other models, the mesopores are generated such that they are separate bodies, including the model with mesopores of 40µm radius (Figure 17e) which have a minimum separation distance of a single grid voxel (Table 4). As such the connectivity between the mesopores in the models with mesopores of 40µm radius or less, is determined by the presence of microporosity, a shown in the cross-section through the 30µm radius model (Figure 17d). This style of connectivity is observed in epoxy resin cast images (Figure 1b) and additionally, the moldic mesopore in Figure 1b shows a rough topography around its perimeter which is caused by micrite. This rough topography is captured by the model, again, as shown in Figure 17d.

3.3.2.   Pore Network Properties

As stated previously the mesopores in the first four models are very well connected by microporosity (Figure 17d), without which, they would otherwise be isolated. This variation in connectivity with mesopore separation (and size) is best examined using the average and maximum coordination numbers (Figure 18).

Upon introduction of the mesopores (10µm radius) to the micritic matrix, the average coordination number for each model increases and then progressively decreases with increasing mesopore radius (Figure 18a). The increase in average coordination number is because the 10µm radius mesopores connect to a large number of micropores initially. However, as the mesopores increase in size, there are more micropores connected to the mesopore edge (increase in maximum coordination number, Figure 18b) and each micropore that connects to a mesopore has, on average, half of the 3D possible

23

574 connections by connecting to a single mesopore rather than potentially being connected to

575 multiple additional micropores, as those found in the centre of the micropore matrix do.

576 Hence, the average coordination number decreases. However, the variation in average

577 coordination for each matrix porosity is only 0.1. The average coordination number is

578 calculated by frequency of occurrence and as such is dominated by the most common

579 pore size, here, microporosity. Although pores with larger and larger coordination numbers

580 are present as mesopore radii increases, the coordination number is still dominated by the

581 microporosity whose presence decreases with increased mesopore radius.

582 As would be expected, the maximum coordination number for the models was found to

583 decrease with increasing matrix porosity (Figure 18b) and increase with mesopore radius

584 such that the maximum coordination number exceeded 1300 in the 40μm radii mesopore

585 model with 18% matrix porosity (Figure 18b). The maximum coordination number

586 decreases for 45μm radii mesopores because these pores are overlapping and as such

587 are not entirely surrounded by microporosity, reducing the maximum coordination number.

588 ### 3.3.3.   Porosity and Single-phase Permeability

589 As mesopore radius increases, the relative proportion of the total porosity that is

590 microporosity within the models decreases (Figure 19a) and as would be expected the

591 overall effect of the presence of mesopores within a microporous matrix is to increase

592 single-phase permeability (Figure 19b). However, lattice-Boltzmann flow simulations also

593 indicate that the impact of the presence of mesopores on single-phase permeability varies

594 depending on the porosity of the microporous matrix: a lower porosity matrix experiences a

595 larger increase in single-phase permeability upon the introduction of mesopores into the

596 model. While the mesopores are unconnected (up to a radius of 40μm), models with a

597 matrix porosity of 18% experience a full order of magnitude increase in permeability while

598 those with a higher matrix porosity experience an increase of less than an order of

24

599   magnitude.

600   Additionally, as the mesopore size increases, the variation in permeability with matrix

601   porosity also decreases, as indicated by the black boxes in Figure 19b: the spread of

602   permeabilities is lower for large mesopores than for smaller or no mesopores showing that

603   increasingly larger mesopores influence flow more relative to the matrix flow. Upon

604   connection of the mesopores at 45μm radius, all models see three orders of magnitude

605   increase in permeability as would be expected for a straight capillary tube. Due to the

606   larger capillary pressure required to simulate flow in the micropores compared to the

607   macropores, no such flow takes place, and as such, in these models flow completely

608   bypasses microporosity.

609   ### 3.3.4.   Multi-phase Flow

610   From Figure 20 and Figure 21 it is clear that the presence of mesopores within the

611   microporous matrix, and indeed the different sizes of mesopores, greatly impact multi-

612   phase flow. The multi-phase flow properties can be seen to vary significantly across the

613   range of models generated.

614   Since the 45μm radii mesopore model is purely conceptual, its multi-phase flow results are

615   illustrated for drainage only to show the change in behaviour through connected

616   mesopores. For all other models during drainage, with increasing mesopore size (direction

617   of arrow) there is a decrease in oil relative permeability at the same saturation (the

618   opposite trend can be seen in the water relative permeability curves). This occurs because

619   the larger mesopores are filled with oil quicker than the smaller mesopores as they are

620   separated by thinner zones of micropores. When these mesopores are filled, the water

621   saturation decreases hugely, however there is still no permeable pathway from inlet to

622   outlet so the relative permeability of oil remains lower than in the smaller mesopore

623   models. This process is also linked to the trend that as mesopore radius increases, the

25

relative permeability curves become more step-like. This is best observed for the 30µm mesopore model water relative permeability curve (Figure 20g) and indicates a more heterogeneous pore system and the successive invasion of mesopores with oil. Sections of the curve with a much steeper gradient indicate slow drainage (a slower decrease in water saturation) as the oil is forced through the microporous horizons between mesopores. Sections of the curves with a much shallower gradient (boxes) indicate a sharp decrease in water saturation and the drainage of oil into a mesopore.

During water wet imbition, these step wise relative permeability curves are not observed and this is related to trapping. During imbition the smallest pores fill first which, due to the fabric of the models, results in a connected pathway from inlet to outlet through the micropores, bypassing the mesopores. As such, the oil filled mesopores become trapped, never being drained of their oil and the step wise saturation changes are not observed. This trapping effect results in an increase in residual oil with increasing mesopore size, where the volume of the pore system contained within the mesopores increases (Figure 22a). In other words, with an increase in homogeneity (more pores of a single type, here micropores, fewer mesopores) there is an improved sweep. Residual oil can also be seen to decrease with an increase in matrix porosity (Figure 21b,e,h and Figure 22).

The water-wet imbition results for the models with 40µm radius mesopores, however, disregard this trend and this is thought to be because the pores are only disconnected from the outlet by a single row of voxels. As such, when merged with the microporous matrix, some of the mesopores then become directly connected to the outlet and are able to drain of oil, considerably decreasing residual oil saturation. This effect is interesting but it should be noted that such models are not representative elemental volumes as the number of unconnected mesopores may decrease to one, or even zero.

Under a fractionally oil wet imbition scenario, quite the opposite trend can be observed.

649 With increasing mesopore radius, a decrease in residual oil occurs (Figure 21c,f,i and

650 Figure 22b). As mentioned earlier, under a fractionally wet scenario the oil wettability is

651 randomly distributed amongst 50% of the pores, independently of any of their physical

652 properties (shape, size etc). As such, statistically, half of the mesopores will be oil wet

653 allowing the development of oil films and oil drainage can continue from some mesopores

654 even while water saturation is high. As mesopore size increases, the relative proportion of

655 oil that can be drained through oil wet mesopores increases and so residual oil is lower for

656 models with larger mesopores (Figure 21f&i). Of course, this is a statistical distribution of

657 wettability and as such some models do not conform to this trend (e.g. Figure 21c, 30µm

658 radii model).

659 **4. Discussion**

660 By investigating the effect of micropore size (Section 3.1) and total microporosity (Section

661 3.2) it has been shown that the new object based rock reconstruction algorithm used to

662 model chalky microporous carbonate fabric is able to capture the basic textural properties

663 that control the macro-scale single-phase permeability in these rock fabrics. There is a

664 very good match between modelled single-phase permeability and the experimental

665 porosity-permeability data (Figure 14a) reported for the chalky microporous facies of the

666 Middle Eastern Lower Cretaceous Shuaiba formation (Fullmer et al., 2014). Additionally,

667 the morphology of the modelled crystal fabrics are reasonable when compared to real

668 rocks (Figure 5).The assumption that chalky micropores are so small that the capillary

669 pressures are too high for oil to be have also proven incorrect by this study. The capillary

670 pressure curves in Figures 10, 16 and 21 show ranges that are not out with the range

671 expected within reservoirs.

672 We have aimed to represent some of the different fabrics of microporous carbonates by

673 varying micropore size, total microporosity, crystal shape due to micritic dissolution and the

presence of mesopores within the matrix, all of which can be observed in nature through sample analysis. Since modelling chalky micropores requires sub-micron resolution, being able to either observe or represent the micropores within a multiscale network is a formidable challenge. Indeed, in all digital rock reconstructions there is a trade-off between the spatial resolution of the model and the largest (or smallest) scale of features that can be examined. The upper limits of computational power and memory restrict firstly the number of voxels in a model volume and therefore the physical volume of a model that can be created, and secondly restrict the grid volume through which fluid flow can be simulated. As such, while a higher spatial resolution of model allows features to be more finely resolved, a higher resolution significantly reduces the physical model size that can be held within the memory limits of the machine being used since the 3D model size increases as the cube of the number of voxels along each axis.

While examining the effect of micropore size it has been observed that the micropores in models generated between 0.10-0.40μm^3/voxel resolution have very similar single- and multi-phase flow behaviour. This result suggest that models generated at a resolution of 0.40μm^3/voxel are able to represent the same physical pore scale flow as models generated at 0.10μm^3/voxel, a resolution which is much closer to the size of chalky micropores observed in epoxy resin casts (Figure 1b). Indeed, the single-phase permeability match with experimental data reported in Section 3.2 further corroborates that modelling the microporous fabrics at a resolution of 0.40μm^3/voxel captures the relevant pore scale features that exist within real chalky microporous carbonate fabrics.

However, models generated at a resolution of 0.50μm^3/voxel exhibited different pore network and multi-phase fluid flow properties. In comparison to these at higher resolutions models at 0.50μm^3/voxel showed a larger percolation radius (Figure 7) and quite different water relative permeability behaviour during imbibition (Figure 9), which resulted in a lower residual oil saturation (Figure 10). It is difficult to determine the exact reasons for this

700 change in residual oil, however it is likely to be due to the larger volume of the pore

701 network contained in the modal pore size within this model and also due to the increased

702 percolation threshold which will reduce trapping. These results tend to suggest that a

703 tipping point in the multi-phase flow properties of micropores falls between those with a

704 modal size range of between $0.40\mu m^3$/voxel and $0.50\mu m^3$/voxel. Below $0.40\mu m^3$/voxel the

705 multi-phase flow properties are similar while above $0.40\mu m^3$/voxel, the multi-phase flow

706 properties vary quite significantly. Interestingly though, the $0.50\mu m^3$/voxel resolution model

707 did not exhibit a distinct increase in single-phase permeability, and all of the different

708 resolution models have very similar single-phase permeability properties (Figure 8). The

709 distinct change in percolation threshold and connectivity of the $0.50\mu m^3$/voxel model

710 (Figure 7) has little effect on single-phase permeability in comparison to the other

711 resolution models.

712 These results provide the ability to model larger physical volumes, and to incorporate

713 chalky microporosity into a more multiscale network, by modelling at a resolution of

714 $0.40\mu m^3$/voxel. At this resolution it was shown that volume of microporosity affects single-

715 phase permeability by an order of magnitude (0.6mD to 7.5mD) over the range of

716 porosities examined (18-35%, Figure 14) but that increasing matrix porosity has very little

717 effect on multi-phase relative permeability and residual oil saturation under both the

718 strongly water wet and fractionally wet wettability scenarios (Figure 15). The effect of

719 micrite rounding due to dissolution has also been examined here. Comparing a rhombic

720 matrix to its rounded counterpart (dashed lines, Figure 14b) shows an increase in porosity

721 of 7-8% (which is in agreement with the increase in porosity due to rounding reported by

722 Lambert et al. (2006)) and also a substantial increase in single-phase permeability, up to

723 an order of magnitude for the lowest porosity models. As such, if a reservoir was of

724 constant volume microporosity within the rhombic fabrics, rounding of the original fabric

725 (most probably toward the top of the oil column) would result in a stratigraphic alteration of

726 the single-phase permeability due to the increase in porosity, as indicated by these results

727 and in agreement with Lambert et al. (2006). It is interesting to note, however, that the

728 overall effect of micritic dissolution on the single-phase and multi-phase permeability

729 trends appears to be limited. At approximately the same porosity (30%, indicated by the

730 arrows in Figure 14b), the permeability in a rounded micrite model can be seen to be only

731 slightly higher (~1mD) than in a rhombic crystal model. This is also shown in the multi-

732 phase flow results (Figure 15) which indicate that micrite dissolution and rounding has very

733 little effect on multi-phase flow under these wettability scenarios. It appears that rounding

734 the micrite crystals has little to no effect on the pore network topology in comparison to the

735 pore networks within rhombic micrite and hence little change in the multiphase flow

736 properties.

737 At a resolution of $0.40\mu m^3$/voxel it is possible to include up to three orders of magnitude of

738 pore size variation through the inclusion of meso-scale pores (>10μm diameter). Results

739 have shown that the addition of mesopores to a micritic matrix greatly impacts the

740 geometry and topology of the pore system (Figure 18) and the single-phase permeability

741 of the models increases with increasing mesopore radius (Figure 19). The relationship

742 between single-phase permeability and mesopore radius is non-linear but is related to the

743 separation distance between the mesopores and therefore the proportion of microporosity

744 within the models. Here microporosity dominates single-phase permeability where it

745 provides the only permeable connection between mesopores (mesopores with a radius of

746 10-30μm) and single-phase permeability is limited to less than 20mD. A distinct increase in

747 single-phase permeability for models with mesopores of 40μm radii is due to the single

748 voxel separation between the mesopores: at such small separation distances the

749 mesopores may be connected by a single or a few micropores and as such the

750 permeability becomes dominated by the mesopores. This is the same for models with

751 mesopores of 45μm radius, where the flow is able to completely bypass the microporosity

752   and permeability thus increases by three orders of magnitude.

753   The multi-phase flow properties of the models also vary significantly with both mesopore

754   size and matrix porosity and it has been shown that these results are again related to the

755   separation distance between mesopores and the relative proportion of microporosity in the

756   models. Most importantly, under a water wet imbibition scenario, an increase in

757   homogeneity (more micropores, fewer mesopores) increases the sweep of the model

758   (Figure 22a). This increase in sweep with homogeneity has been reported by other authors

759   in fabrics where micropores are present (Hollis et al., 2011; Fullmer et al., 2014) and is

760   also observed in the water wet imbibition capillary pressure curves in Figure 21b, e & h.

761   We are aware that in reality not all mesopores in a reservoir have the same shape and

762   size. Here, the mesopore models are entirely synthetic and the porosities of the models

763   with the largest mesopores are beyond the porosities typically observed in these types of

764   carbonates (Figure 19a). Yet this study has demonstrated the flexibility of the developed

765   algorithm to explore these variations and provides a basis to further develop future studies.

766   By methodologically altering certain parameters of the porous fabrics (crystal packing,

767   crystal size, porosity, mesopores) and also the properties of fluids simulated, it will be

768   possible to build a state-space of how the properties of microporous carbonates vary

769   under these different fabrics and use the trends to predict single-phase and multi-phase

770   flow.

771   Finally, across all different fabrics it has been shown that the wettability scenario modelled

772   during imbibition impacts the residual oil. The wetting state of any rock is extremely hard to

773   determine as core wettability experiments are expensive (both in time and money), and

774   more importantly it is difficult to ensure that the core wettability under lab conditions is the

775   same as in-situ subsurface conditions. Relative permeability data are therefore difficult to

776   acquire under reservoir conditions. If such data are available, they are usually only for one

777 particular bulk plug sample while the wetting state of a carbonate may vary at a much

778 smaller (pore scale) and indeed larger scales. Modelling two phase flow under a variety of

779 different wettability scenarios is one possible way to understand how the fluid flow

780 properties would vary under different wetting states and this wettability dependent variation

781 in multi-phase flow properties and residual oil has been demonstrated in this study by

782 looking at strongly wet imbibition and fractionally oil wet imbibition. The multi-phase flow

783 results for models with varying sizes of mesopores demonstrates the dependency of

784 recovery on wetting scenario (Figure 22).

785 However, the wetting state of a real rock is not randomly distributed throughout the pore

786 network as is simulated for the fractionally wet wettability case here. Intermediate

787 wettability (where part of the pore system is oil-wet and the remainder oil-wet) maybe

788 controlled by the pore size or pore shape (degree of curvature), or wettability is controlled

789 by mineralogy (Kovscek et al., 1993; Skauge at al., 2004). The mineralogy of the micrite in

790 these microporous carbonate models does not vary, and as such mineralogy does not

791 need to be considered as a controlling factor on wettability alteration. Pore size and shape,

792 however, are viable controls on wettability at the pore scale. While network models are

793 able to determine wetting alteration due to pore size, they are not able to model wettability

794 alteration due to changes in pore shape/curvature as defined by the extracted pore

795 network. Blunt (1998) introduced a model capable of modelling wettability based on pore

796 shape parametrically but a network model flow simulator capable of modelling fluid layers

797 that are dependent on pore shape as defined in the pore network, is vital if we are to be

798 able to predict multi-phase flow properties of carbonates and indeed, other media. Under a

799 wetting state controlled by pore shape, the multi-phase properties of rounded micrite

800 compared to rhombic micrite may indeed be very different as although the structure of the

801 pore network has been seen to vary only slightly in this study, the largest effect of micrite

802 rounding could be on pore shape.

5. Conclusions

We present a flexible object-based rock reconstruction algorithm that reproduces the fabric of chalky microporous carbonates. We apply the algorithm to probe the effects of micropore size, total microporosity and micritic dissolution on both single- and multi-phase fluid flow properties within a purely micritic matrix. The algorithm is also used to examine the effect of the presence of mesopores of varying sizes within a micritic matrix on both single- and multi-phase flow.

Micropore size (controlled by varying model resolution) was found to have little to no effect on single-phase permeability within the range of resolutions modelled here (0.10-0.50μm^3/voxel). However a tipping point in the multi-phase flow properties has been observed for microporous fabrics with pores no smaller than 0.50μm^3, which exhibit quite different flow properties to those with smaller sizes. We conclude that voxels and pores at least as small as 0.40μm^3 for such modelling.

Total microporosity has been shown to influence single-phase permeability significantly and over the range of porosities modelled (18-35%) an order of magnitude increase on permeability occurs. These results indicate that microporosity can conduct significant single-phase permeabilities of up to 7.5mD which is in agreement with literature reported experimental data. Total microporosity was however shown to have little to no effect on multi-phase flow behaviour and oil recovery in these models.

The algorithm is capable of mimicking micritic dissolution (rounding) and results indicate that rounded micritic fabrics have a considerable effect on the porosity (increase of up to 8%) and single-phase permeability (increase of up to order of magnitude) in comparison to their original rhombic micritic fabrics, while the overall porosity-permeability trends exhibit only slight increase in permeability at a given porosity suggesting that the pore network topology is not significantly altered by rounding. Additionally, multi-phase flow properties

828 remain unaltered between the rhombic crystal fabric and the rounded model fabric.

829 Finally it has been shown that the presence of mesopores within a micritic matrix can

830 greatly impact flow properties after they become directly connected, but if they are

831 disconnected single-phase permeability is controlled by micropores and only an order of

832 magnitude variation in permeability is observed with varying microporosity. Indeed, these

833 fabrics have been shown to be able to conduct significant permeabilities of up to 20mD

834 while the mesopores are unconnected, demonstrating that microporosity cannot simply be

835 overlooked within multiscale carbonate pore systems. Additionally, it has been shown that

836 fabrics with a higher fraction of total porosity that is microporosity retain a much lower

837 residual oil saturation during water wet imbibition. Under this wettability scenario, the

838 presence of microporosity within a carbonate reservoir is desirable, as it increases the

839 sweep of the reservoir during imbibition.

840 Carbonate microporosity is found within many different rock fabrics and often in

841 combination with other scales of porosity. This study has examined only a small sector of

842 the spectrum of fabric variation and indeed the different hypothetical wettability scenarios,

843 but has shown the breadth of single-phase flow properties and more importantly multi-

844 phase flow properties that can occur through these fabrics. When assessing the

845 producibility of microporous carbonates it is therefore important to consider the

846 microporosity and understand its role in fluid flow through the fabrics present. The

847 algorithm developed here provides a flexible platform with which to probe the full spectrum

848 of variations of microporous fabrics and different geologically controlled wettability

849 scenarios.

850 **References**

851 Al-Kharusi, A.S., and Blunt, M.J., 2008, Multi-phase flow predictions from carbonate pore

852 space images using extracted network models, Water Resources Research, V.44

853 Bakke. S., and Øren. P-E., 1997, 3-D Pore-Scale Modelling of Sandstones and Flow

854 Simulations in the Pore Networks, SPE Journal, v. 2.

855 Biswal. B., Øren. P-E., Held. R., Bakke. S., and Hilfer. R., 2007, Stochastic multiscale

856 model for carbonate rocks, Physical Review E 75, 061303.

857 Biswal. B., Held. R.J., Khanna. V., Wang. J., and Hilfer. R., 2009a, Towards precise

858 prediction of transport properties from synthetic computer tomography of reconstructed

859 porous media, Physical Review E 80, 041301.

860 Biswal. B., P-E Øren., Held. R., Bakke. S., and Hilfer. R, 2009b, Modelling of multiscale

861 porous media, Image Analysis and Stereology 28, p23-34.

862 Blunt, M., 1998, Physically-based network modelling of multiphase flow in intermediate-wet

863 porous media, Journal of Petroleum Science and Engineering, 20, p117-125

864 Bobek, J. E., Mattax, C. C., and Denekas, M. O., 1958, Reservoir Rock Wettability - Its

865 Significance and Evaluation, Society of Petroleum Engineers.

866 Budd, D., 1989, Micro-rhombic calcite and microporosity in limestones: a geochemical

867 study of the lower cretaceous Thamama group, UAE, Sedimentary Geology, v. 633-4,

868 p293-311.

869 Cantrell, D. L. and Hagerty, R. M., 1999, Microporosity in Arab formation carbonates,

870 Saudi Arabia, GeoArabia 4, p129 - 154.

871 Chilingar, G.V. and Yen, T. F., 1983, Some Notes on Wettability and Relative Permeabilities

872 of Carbonate Reservoir Rocks, II, Energy Sources, Vol. 7.

873 Choquette, P., and Pray, L., 1970, Geologic Nomenclature and Classification of Porosity in

874 Sedimentary Carbonates, AAPG Bulletin, v. 542, p207-250

875 Chun, B. and Ladd, A. J. C., 2007, Interpolated boundary condition for lattice Boltzmann

876 simulations of flows in narrow gaps, Phys. Rev. E 75

877   Cox, P., Wood, R., Dickson, J.A.D., Al-Rougha, H.B., Shebl, H., and Corbett, P.W.M., 2010,

878   Cynamics of cementation in response to oil charge: Evidence from a Cretaceous

879   carbonate field, U.A.E., Sedimentary Geology, v228(3-4), p246-254

880   Cuiec, L., 1984, Rock/crude-oil interactions and wettability: An attempt to understand their

881   interrelation, Society of Petroleum Engineers, Vol. 13211

882   Darcy, H., 1856, Les Fontaines Publiques de la Ville de Dijon, Dalmont, Paris

883   Desplat, J. C., Pagonabarraga, I., and Bladon, P., 2001, LUDWIG: A parallel Lattice-

884   Boltzmann code for complex fluids, Computer Physics Communications, v. 1343. p273-

885   290

886   Deville de Periere, M., Durlet, C., Vennin, E., Lambert, L., Bourillot, R., Caline, B., and Poli,

887   E., 2011, Morphometry of micrite particles in cretaceous microporous limestones of the

888   Middle East: Influence on reservoir properties, Marine and Petroleum Geology, 289,

889   p1727-1750.

890   Dravis, J.J., 1989, Deep-burial microporosity in upper Jurassic Haynesville oolitic

891   grainstones, East Texas, Sedimentary Geology, Volume 63, Issues 3–4, Pages 325-341.

892   Folk, R. L., 1962, Classification of carbonate rocks, AAPG memoirs, 1, p62-84.

893   Fullmer, S. M., Guidry, S. A., Gournay, J., Bowlin, E., Ottinger, G., Al Neyadi, A. M., and

894   Edwards, E., 2014, Microporosity: Characterization, Distribution, and Influence on Oil

895   Recovery, International Petroleum Technology Conference Abstract.

896   Heasley, E.C., Worden, R.H., and Hendry, J.P., 2000, Cement distribution in a carbonate

897   reservoir: recognition of a palaeo oil–water contact and its relationship to reservoir quality

898   in the Humbly Grove field, onshore, UK, Marine and Petroleum Geology, Volume 17, Issue

899   5, p639-654

900   Hollis, C., Vahrenkamp, V., Tull. S., Mookerjee. A., Taberner. C., and Huang. Y., 2011, Pore

system characterization in heterogeneous carbonates: An alternative approach to widely-used rock-typing methodologies, Petroleum Geoscience 27, p772-793.

Jiang, Z., Wu, K., Couples, G.D., van Dijke, M.I.J., and Sorbie, K.S., 2007, Efficient extraction of networks from 3D porous media, Water Resource Research, 43, W12S03.

Kashfi, M., 1974, A Brief Study of Reservoir Rock Wettability in the Iranian Oil Fields, Energy Sources, Vol. 1

Kirkham, A., Bin Juma, M., McKean, T.A.M., Palmer, A.F., Smith, M.J., Thomas, A.H., and Twombley, B. N., 1996, Fluid saturation prediction in the 'transition zone' carbonate reservoir, Abu Dhabi, Geoarabia 1, p551-566

Kovscek, A.R., Wong, H., and Radke, C.J., 1993, A pore-level scenario for the development of mixed wettability in oil reservoirs, AIChE Journal, 39(6), p1072-1085

Lambert, L., Durlet, C., Loreau, J.-P. and Marnier, G., 2006, Burial dissolution of micrite in Middle East carbonate reservoirs Jurassic-Cretaceous: keys for recognition and timing, Marine and Petroleum Geology 231, p79-92.

Lucia, F.J. and Loucks, R.G., 2013, Micropores in carbonate mud: early development and petrophysics, GCAGS Journal, Volume 2, p1-10

Morrow, N. R., 1976, Capillary Pressure Correlations for Uniformly Wetted Porous Media, Petroleum Society of Canada

Moshier, S., 1989a, Development of microporosity in a micritic limestone reservoir, lower cretaceous, Middle East, Sedimentary Geology 633-4, p217-240

Moshier, S. O., 1989b, Microporosity in micritic limestones: a review, Sedimentary Geology 63, p191-213.

Okabe, H., and Blunt, M., 2004, Prediction of permeability for porous media reconstructed using multiple-point statistics, Physical Review E, 70, 066135

925 Øren. P-E., Bakke. S., and Arntzen, O., 1998, Extending predicative capabilities to network

926 models, SPE Journal 3, 324-336

927 Øren. P-E. and Bakke. S., 2003, Reconstruction of Berea sandstone and pore-scale

928 modelling of wettability effects, Journal of Petroleum Science and Engineering 39, p177–

929 199

930 Pittman, E. D., 1971, Microporosity in Carbonate Rocks: geological notes, AAPG Bulletin,

931 5510, p1873-1878.

932 Richard, J., Sizun, J.P., and Machhour, L., 2007, Development and compartmentalisation

933 of chalky carbonate reservoirs: The Urgonian Jura-Bas Dauphine platform model

934 (Genissiat southeastern France), Sedimentary Geology, 198, p195-207

935 Roth. S., Biswal. B., Afshar. G., Held. R., Øren. P-E., Berge. L., and Hilfer. R., 2011,

936 Continuum-based rock model of a reservoir dolostone with four orders of magnitude in

937 pore sizes, AAPG Bulletin, 956, p925-940.

938 Schneider, C.A., Rasband, W.S., and Eliceiri, K.W., 2012, NIH Image to ImageJ: 25 years

939 of image analysis, Nature Methods 9, p671-675.

940 Smith, L. B., Eberli, G. P., Masaferro, J. L., & Al-Dhahab, S., 2003, Discrimination of

941 effective from ineffective porosity in heterogeneous Cretaceous carbonates, Al Ghubar

942 field, Oman, AAPG bulletin, 879, p1509-1529.

943 Sengupta. A., Hammond, P., Frenkel, P., and Boek, E., 2012, Error analysis and correction

944 for Lattice Boltzmann simulated flow conductance in capillaries of different shapes and

945 alignments, Journal of Computational Physics, 231, p2634–2640.

946 Skauge, A., Spildo, K., HØiland, L., Vik, B., and Ottesen, B., 2004, Experimental evidence

947 of different intermediate wetting states, Society of Core Analysts Paper, SCA2004-04

948 Skauge, A., Sorvik, A., Vik, B., and Spildo, K., 2006, Effect of wettability on oil recovery

949 from carbonate material representing different pore classes, Society of Core Analysts

950 Paper, SCA2006-01

951 Torquato, S., 1984, Bulk properties of two-phase disordered media, I. Cluster expansion

952 for the effective dielectric constant of dispersions of penetrable spheres, J Chem Phys 81.

953 5079-5088.

954 Torquato, S., 1985, Bulk properties of two-phase disordered media. II. Effective

955 conductivity of a dilute dispersion of penetrable spheres. J Chem Phys 83, 4776-4785.

956 Torquato, S., 1986, Bulk properties of two-phase disordered media, ill. New bounds 98 on

957 the effective conductivity of dispersions of penetrable spheres, J Chem Phys 84.6345-

958 6359.

959 Treiber, L. E., and Owens, W. W., 1972, A Laboratory Evaluation of the Wettability of Fifty

960 Oil-Producing Reservoirs, Society of Petroleum Engineers

961 Valvatne, P. H., and Blunt, M. J., 2004, Predictive pore-scale modelling of two-phase flow

962 in mixed wet media, Water Resources Research, 407.

963 Van Geet, M., Swennen, R., and Wevers, M., 2000, Quantitative analysis of reservoir rocks

964 by microfocus X-ray computerised tomography, Sedimentary Geology, Volume 132, Issues

965 1–2, Pages 25-36

966 Vogel, H.-J., and Roth, K., 2001, Quantitative morphology and network representation of

967 soil pore structure, Advances in Water Resources, Volume 24, Issues 3–4, Pages 233-242.

968 Volery, C., Davaud, D., Foubert, A., and Caline, B., 2009, Shallow-marine microporous

969 carbonate reservoir rocks in the Middle East: Relationship with seawater Mg/Ca Ratio and

970 eustatic sea level, Journal of Petroleum Geology, Vol.32(4), p313-326

971 Volery, C., Davaud, E., Durlet, C., Clavel, B., Charollais, J., and Caline, B., 2010,

972 Microporous and tight limestones in the Urgonian Formation (late Hauterivian to early

973   Aptian) of the French Jura Mountains: Focus on the factors controlling the formation of

974   microporous facies, Sedimentary Geology, Volume 230

975   Wagner, O., 1990, Geochemical stratigraphy and porosity controls in Cretaceous

976   carbonates ear the Oman mountains, Geological Society, London, Special Publications,

977     $9(1), p127-137

978   Wu, K., Nunan, N., Crawford, J., Young, I., and Ritz, K., 2004, An efficient Markov chain

979   model for the simulation of heterogeneous soil structure, Soil Science Society of America

980   Journal, 68(2), p346

981   Wu, K., van Dijke, M., Couples, G., Jiang, Z., Ma, J., Sorbie, K., Crawford, J., Young, I.,

982   and Zhang, X, 2006, 3D stochastic modelling of heterogeneous porous media applications

983   to reservoir rocks, Transport in Porous Media, v65, p443-476

984   Wu, K., Ryazanov, A., van Dijke, M., Jiang, Z., Ma, J., Couples, G., and Sorbie, K., 2008,

985   Validation of methods for multi-scale pore space reconstruction and their use in prediction

986   of flow properties in carbonate, Society of Core Analysts Paper, SCA 2008-34

Figure 1 Secondary electron SEM images of chalky microporous carbonates. (a) Image of a rough cut chip showing the rhomboidal shape of micrite crystals. (b) Epoxy resin cast showing the sponge like network of microporosity and its connectivity with a larger, meso-scale pore. The inset shows a high resolution image of the plate-like morphology of chalky microporosity between the facets of three micrite crystals. (c) Image of a rough cut chip showing the rounding effect of micritic dissolution: the example highlighted crystals exhibit no vertices or facets.

Figure 2 Example Backscatter SEM images of chalky carbonate microporosity that can be used to extract quantitative data for model calibration. (a) & (b) Typical backscatter SEM images used for crystal diameter measurements. (c) Crystal size distribution as measured from backscatter images and used to populate models at a voxel resolution of $0.4\mu m^3$/voxel.

Figure 3 (a) 100x100voxel slice through a 25% porosity model demonstrating the crystal overlap created by crystal layering. Edge voxels (white) can be seen to overlap or touch one another while individual crystal centres (grey) are entirely separate. (b) Binarised final fabric of the same slice. (c) and (d) show example layered crystal structures of two sizes used in the algorithm (with front-right section removed to show internal layered structure).

Figure 4 Example data from sensitivity tests calculating solid volume loss due to crystal overlap. (a) Sensitivity test data and resultant trend for 400^3 models at a resolution of $0.4\mu m^3$/voxel over a range of porosities. Using the trend it is possible to calculate the model target porosity (ϕ) that should be used in order to achieve any particular required final porosity (ϕ_D). The arrow shows that a target of ϕ=18% should be used to obtain a final porosity ϕ_D=25% (c) These sensitivity tests can be performed for any grid size (three examples are shown) and at any resolution.

Figure 5 Visual comparison between (a) micritic fabrics in a secondary electron SEM image of a rough cut chip and (b) a 300x300voxel slice of a $0.10\mu m^3$/voxel resolution model viewed in pseudo-3D.

Figure 6 400x400 slice of a model at each resolution scaled to relative physical size. $0.50\mu m^3$/voxel through to $0.10\mu m^3$/voxel in (a) through (e) respectively. All models have ~26% porosity.

Figure 7 Pore network properties of different resolution models. Key indicates the voxel resolution of each model. (a) Pore radius distribution. (b) Euler number connectivity function.

Figure 8 (a) Porosities computed from subvolumes at each resolution. (b) Single-

phase permeabilities computed from subvolumes at each resolution. (c) Porosity plotted against single-phase permeability computed for each subvolume (unfilled symbols) and full scale volume realisation (filled symbols).

Figure 9 Relative permeability curves from simulations of multi-phase flow on extracted pore networks within models of varying resolution. Water relative permeability curves are shown as solid lines, oil relative permeability curves are shown as dashed lines. WW= water wet wettability & FW= fractionally wet wettability.

Figure 10 Capillary pressure cures from simulation of multi-phase flow on extracted networks within models of varying resolution.

Figure 11 An example 2D slice through a single realisation of each 3D porosity model. Panels a to e show models of 18% to 35% porosity respectively (refer to Table 3 for exact porosity values). Black voxels indicate pores, while white voxels indicate solid. All slices have dimensions of 400x400 voxels and a resolution of $0.40\mu m^3$/voxel.

Figure 12 A comparison of model fabrics before and after micrite rounding for the 25% porosity model. (a) 100^3 voxel volume of the rhombic crystal model. (b) 100^3 voxel of the rounded crystal model. (c) 100x100 voxel slice of the rhombic crystal model. (d) 100x100 voxel slice of the rounded crystal model. (e) Crystal diameter histogram and cumulative frequency plots for a 400x400 voxel slice of the rhombic and rounded models.

Figure 13 Pore network properties of rhombic models and rounded models. Upper row shows pore radius distributions and lower row shows Euler number connectivity functions. Left hand column shows results for rhombic models, central column shows results for rounded micrite models, and right hand figures show a comparison between the results for 25% porosity rhombic micrite and its resultant rounded micrite fabric counterpart. Keys shown apply to figures directly them.

Figure 14 Porosity against single-phase permeability plots. (a) Rhombic crystal model results plotted with data from Fuller et al. (2014). Modelled fabrics represent those termed Type I by the Fuller et al. scheme. Model data points are an average over three realisations of each model. (b) Comparison between rhombic crystal and rounded crystal porosity-permeability results. Dashed lines trace the transition of the porosity-permeability measurement from the original, rhombic crystal model to its rounded counterpart. Arrows indicate a rhombic crystal model and a rounded crystal model with similar porosities (~30%).

Figure 15 Relative permeability curves from simulations of multi-phase flow on extracted pore networks. Upper row shows results for rhombic crystal models, lower row shows results for rounded crystal models. Water relative permeability curves are shown as solid lines, oil relative permeability curves are shown as dashed lines.

Figure 16 Capillary pressure curves from simulation of multi-phase flow on extracted pore networks. Upper row shows results for rhombic crystal models, lower row shows results for rounded crystal models.

Figure 17 (a) to (c), (e) & (f) show the synthetic moldic mesopore configurations used. (d) Shows a slice through model (c) as indicated by the dashed line in (c) after the mesopores have been combined with 25% matrix porosity model.

Figure 18 Coordination number data for mesopore models. (a) Average coordination number. (b) Maximum coordination number.

Figure 19 Porosity and single-phase permeability plots. (a) Microporosity as a proportion of total porosity. Shading indicates mesopore radii as shown on the plot. (b) Mesopore radius plotted against single-phase permeability. The 0µm radius mesopore (x-axis) data points indicate purely micritic matrix. Boxes highlight the decrease in range of permeabilities with matrix porosity as mesopore radius increases.

Figure 20 Multi-phase flow relative permeability curves for models with varying mesopore radii (see key) and varying matrix porosity. Upper, middle and lower rows indicate models of 18%, 25% and 35% matrix porosity respectively. Arrows indicate direction of increasing mesopore radius for the oil relative permeabilities (dashed lines). Water relative permeabilities are indicated as solid lines. Boxes in (g) indicate fast water drainage in comparison to the slower drainage through steeper curve gradients either side.

Figure 21 Capillary pressure curves for models with varying mesopore radii (see key) and varying matrix porosity. Upper, middle, lower rows indicate models of 18%, 25% and 35% matrix porosity respectively. Arrows indicate direction of increasing mesopore radius.

Figure 22 Plots of mesopore size against residual oil saturation for (a) water wet imbibition and (b) fractionally wet imbibition, under varying matrix microporosity. The direction of arrows indicates direction of decreasing proportion of microporosity.

Table 1 Model resolutions, physical size of full model and number of voxels in each subvolume model.

Table 2 Number of crystals, nodes and bonds, and average pore radius generated at each resolution.

Table 3 Pore network statistics for rhombic crystal models of different porosities and corresponding rounded crystal model (indicated by a and b).

Table 4 Model mesopore radius and corresponding mesopore separation distances.

Resolution (μm^3/voxel)	Full Model Physical Size (μm^3)	Subvolume Model Size (voxels)
0.10	40^3	---
0.20	80^3	200^3
0.30	120^3	133^3
0.40	160^3	100^3
0.50	200^3	80^3

Model Resolution (μm³/voxel)	# Crystals	Average Pore Radius (μm)	# Nodes	# Bonds
0.10	6417	0.26	19270	10491
0.20	39858	0.30	133954	68037
0.30	116407	0.37	283997	141547
0.40	271875	0.38	709514	342223
0.50	495190	0.44	584850	187095

	Model	Porosity %	# Pores	# Throats	# Elements	Average Coordination #	Average Pore Radius (μm)
Rhombic	1a	18.9	303255	576183	879438	3.78	0.329
	2a	21.3	323128	633370	956498	3.91	0.327
	3a	25.6	332709	683879	1016588	4.09	0.336
	4a	30.6	309397	663326	972723	4.27	0.344
	5a	35.7	268670	594955	863625	4.41	0.421
Rounded	1b	27.1	293660	623913	917573	4.23	0.327
	2b	29.6	282337	608558	890895	4.29	0.438
	3b	33.7	249887	547965	797852	4.36	0.543
	4b	38.3	207306	460690	667996	4.42	0.615
	5b	42.9	165973	369289	535262	4.42	0.668

Mesopore Radius (µm)	Minimum Separation (voxels)
10	150
20	100
30	50
40	1
45	0

a 6μm

b Microporosity Mesopore 20μm 5μm

c 4μm
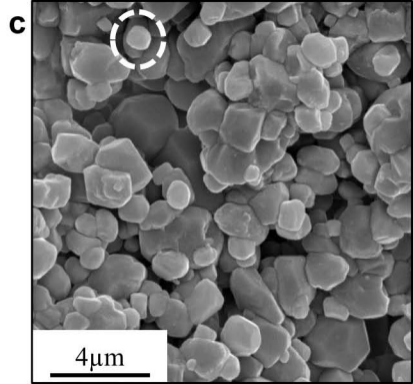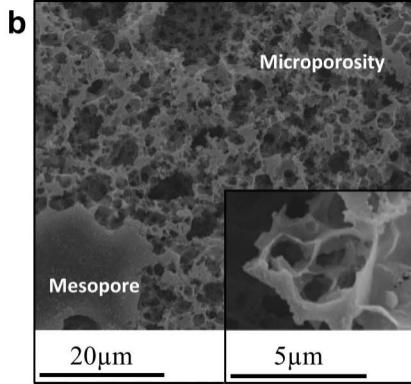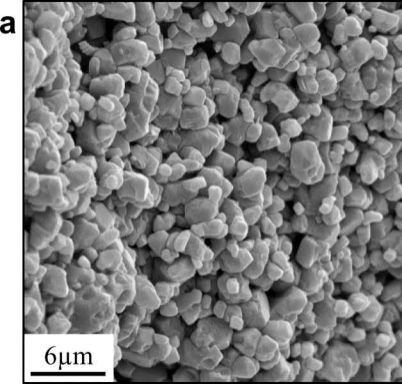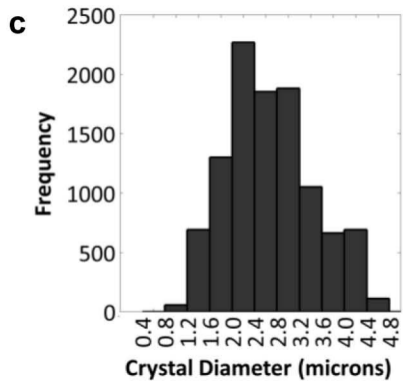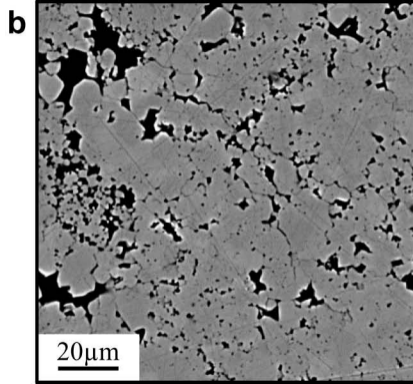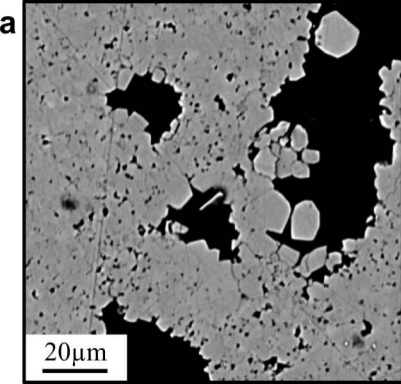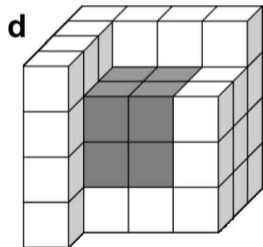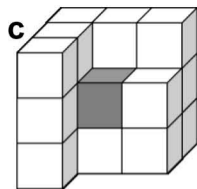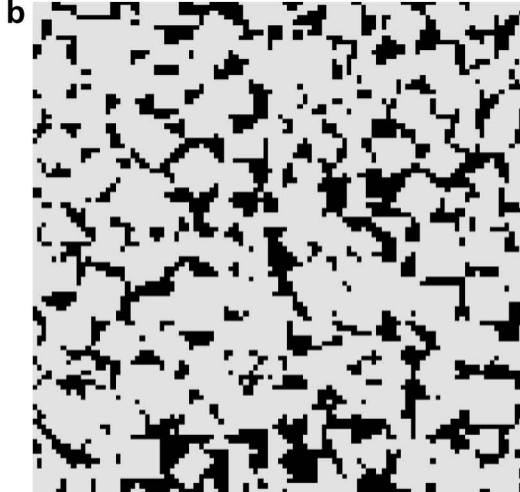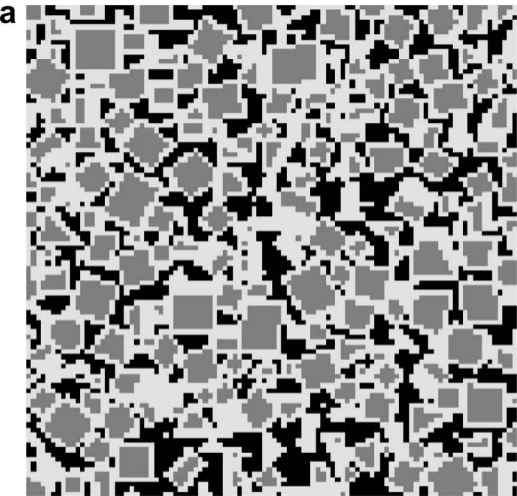
■ Pore	□ Crystal Edge/Overlap layer

Crystal Centre

a 200μm

b 160μm

c 120μm

d 80μm

e 40μm

a   **b**

a

Volume Fraction vs Pore Radius (microns)

b

Euler Number ($\times 10^7$) vs Pore Radius (microns)

Voxel Resolution: 0.1μm, 0.2μm, 0.3μm, 0.4μm, 0.5μm

a

b

c

| **a** | Drainage | **b** | WW Imbibition | **c** | FW Imbibition |

Relative Permeability vs Saturation
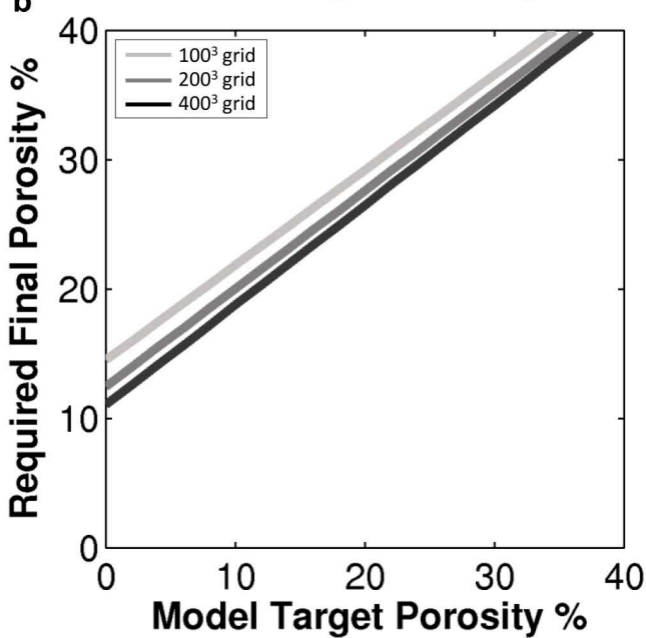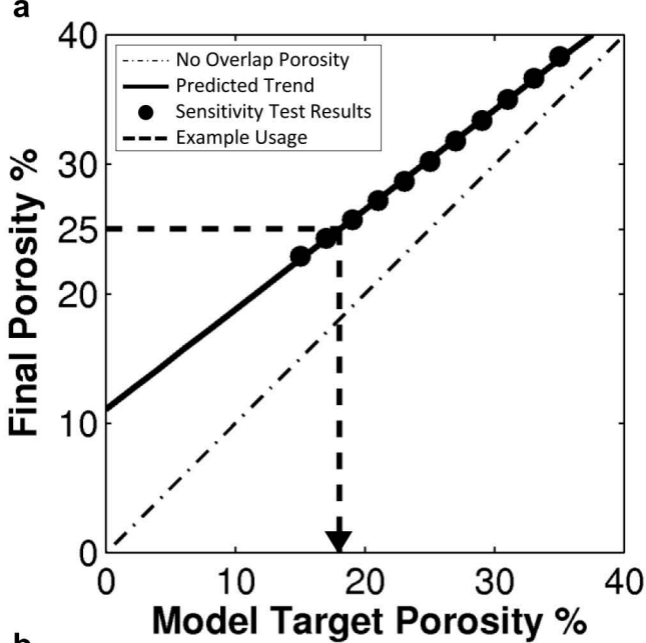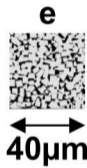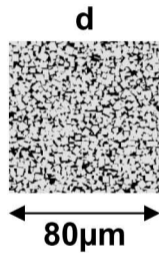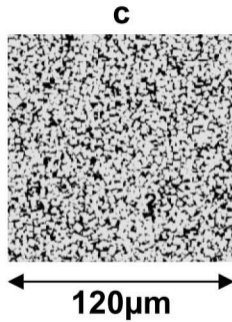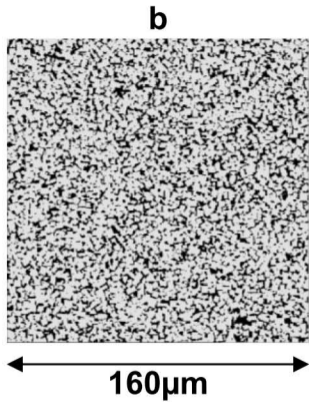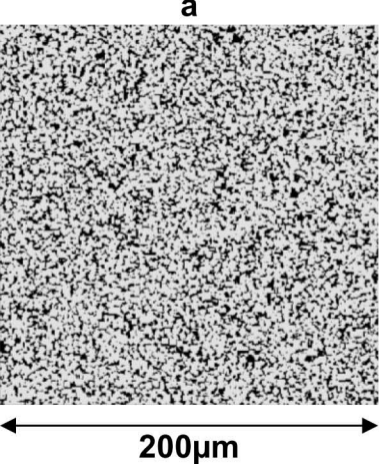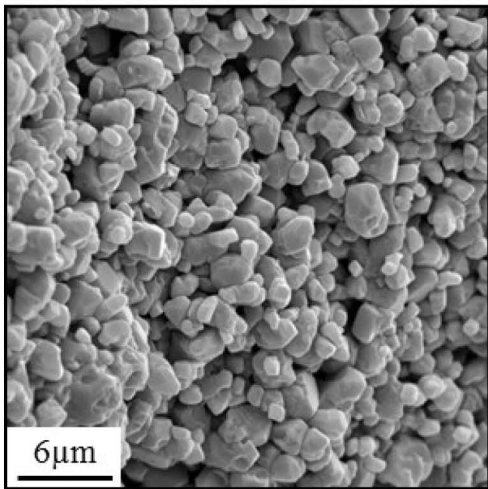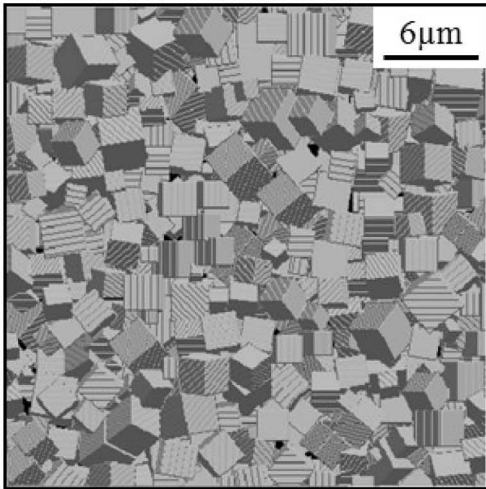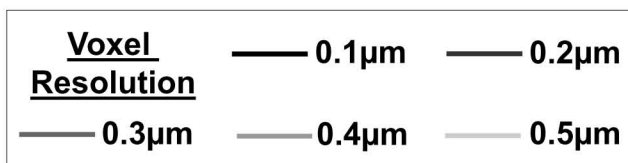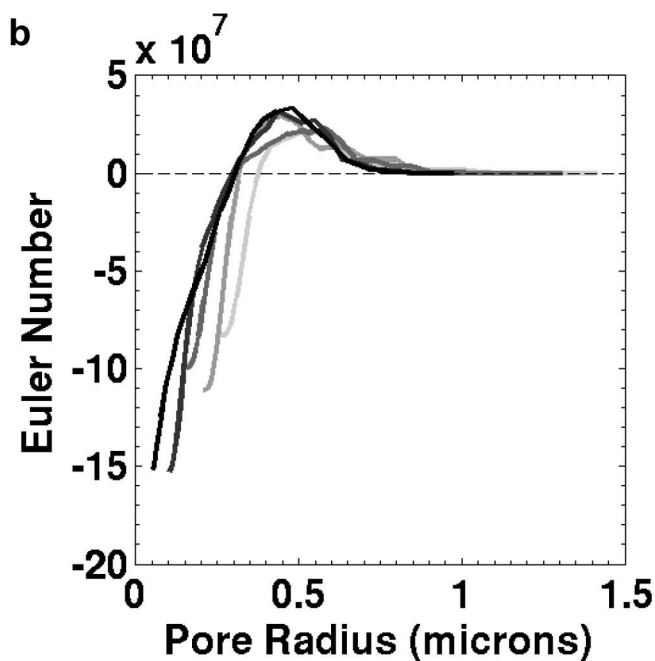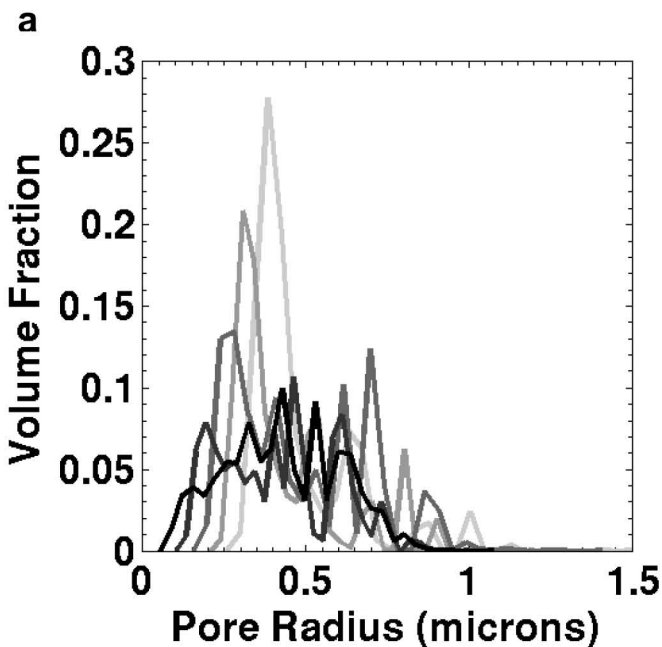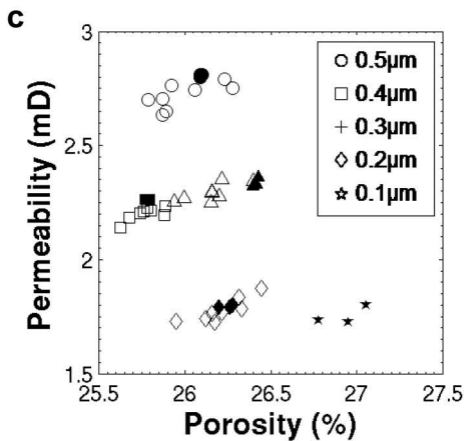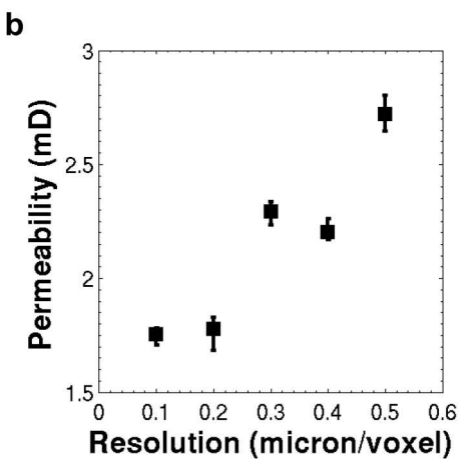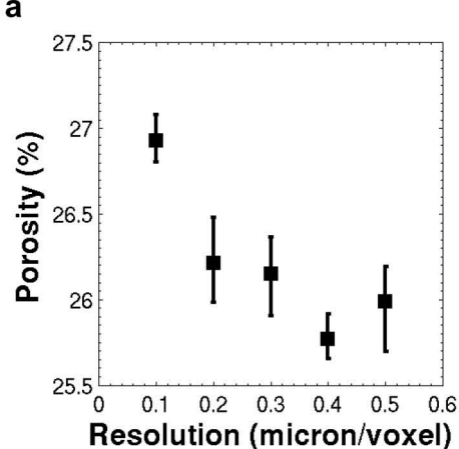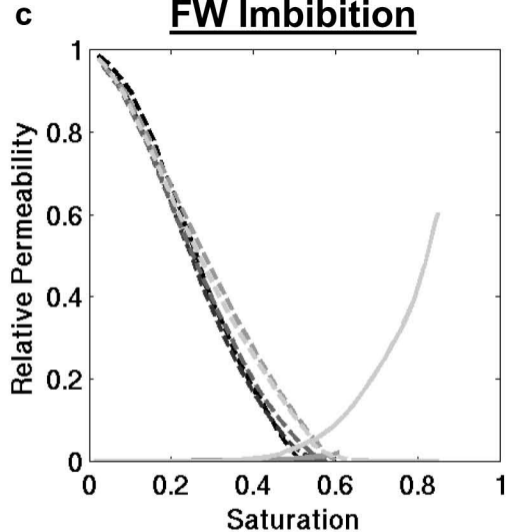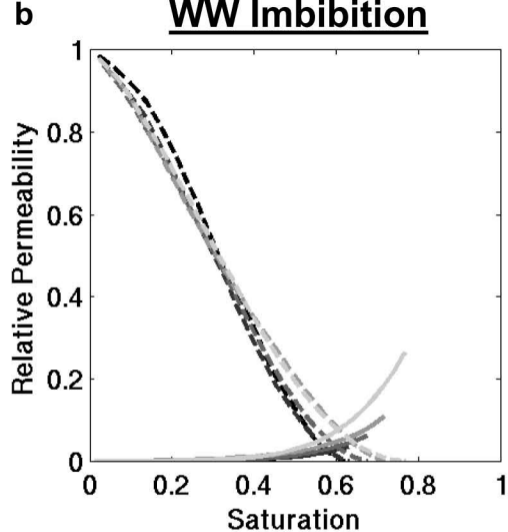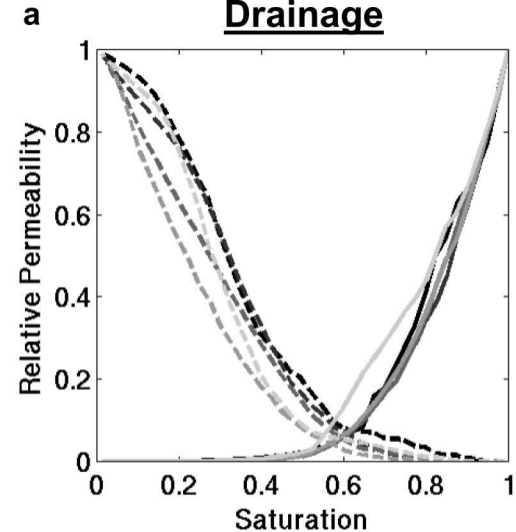
Legend: —— 0.1μm —— 0.2μm —— 0.3μm —— 0.4μm —— 0.5μm

a Drainage
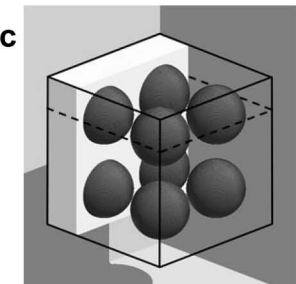
b WW Imbibition

c FW Imbibition

Legend: — 0.1μm — 0.2μm — 0.3μm — 0.4μm — 0.5μm
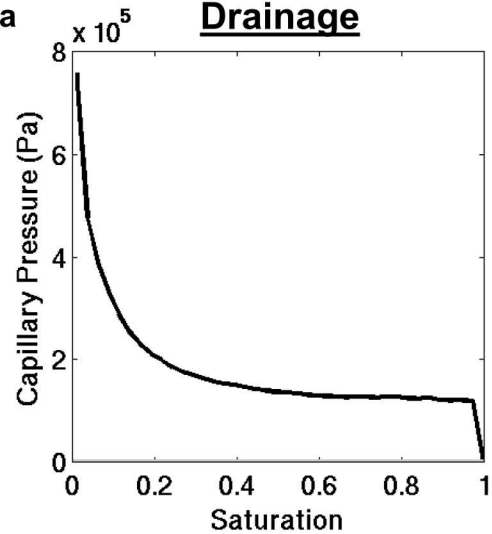
a Rhombic Micrite
b Rounded Micrite
e 25% Rhombic Φ
c
d
f
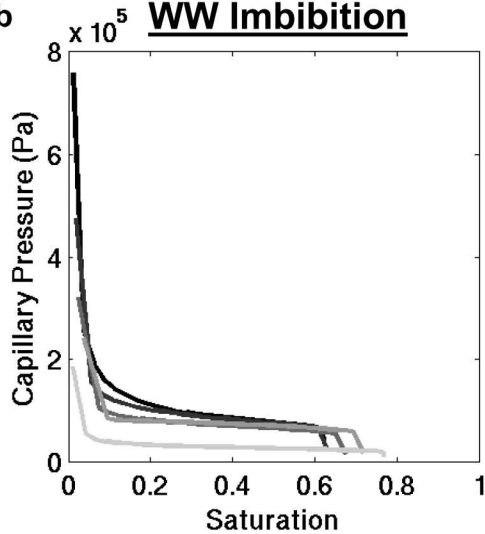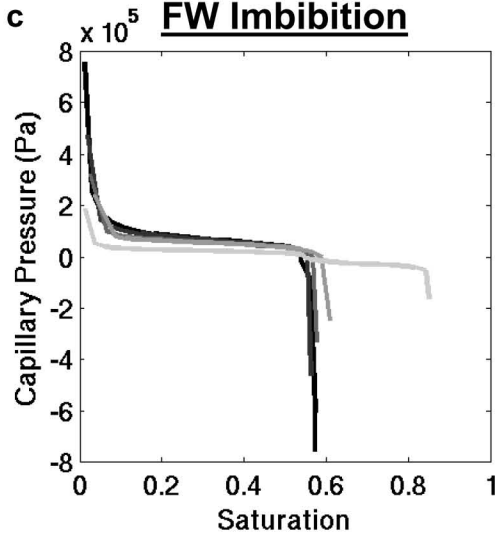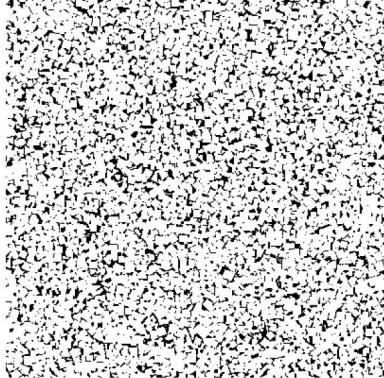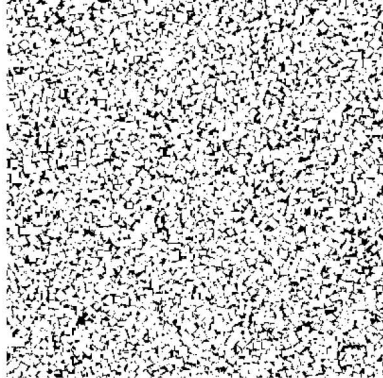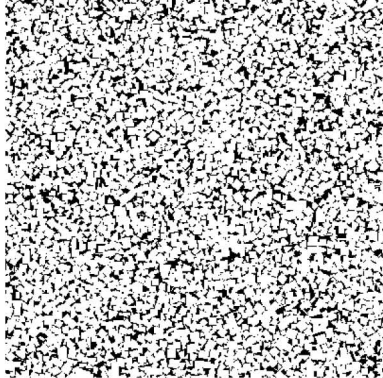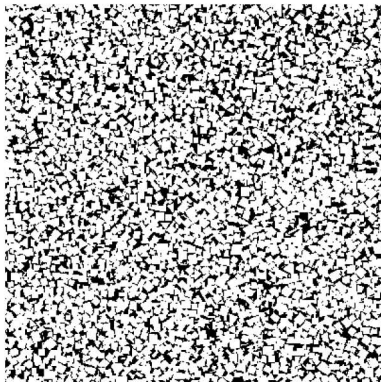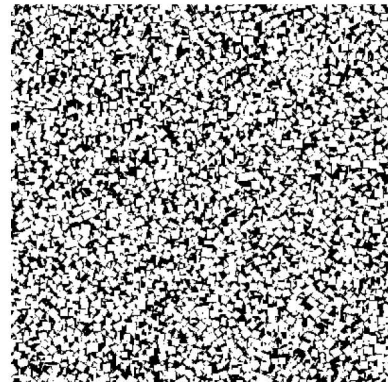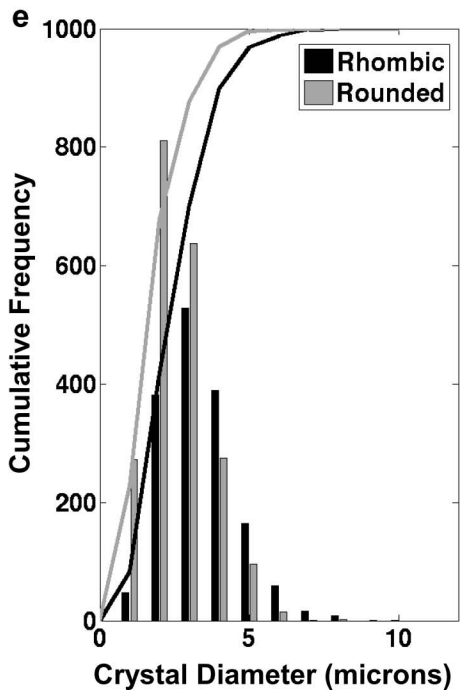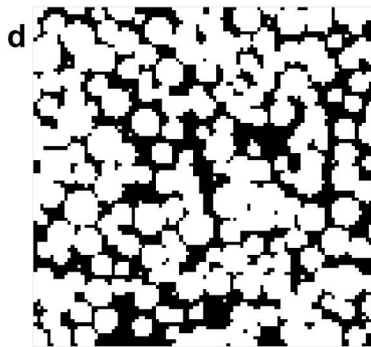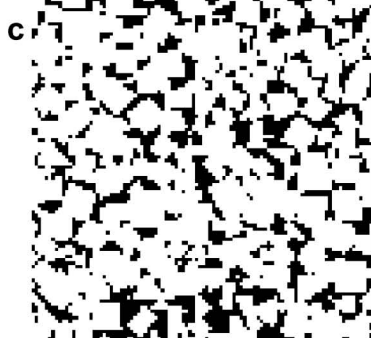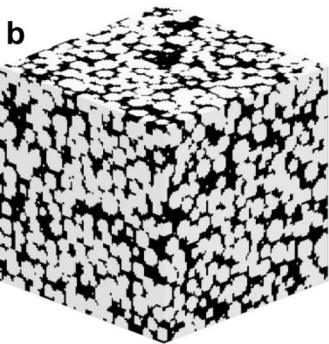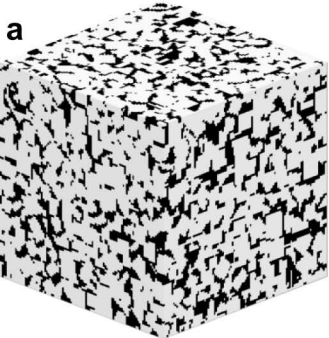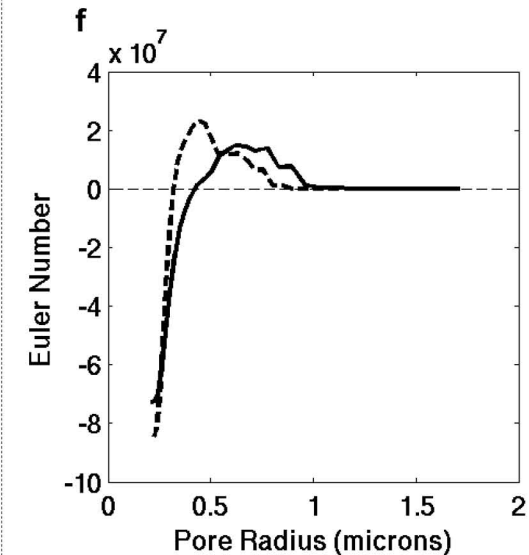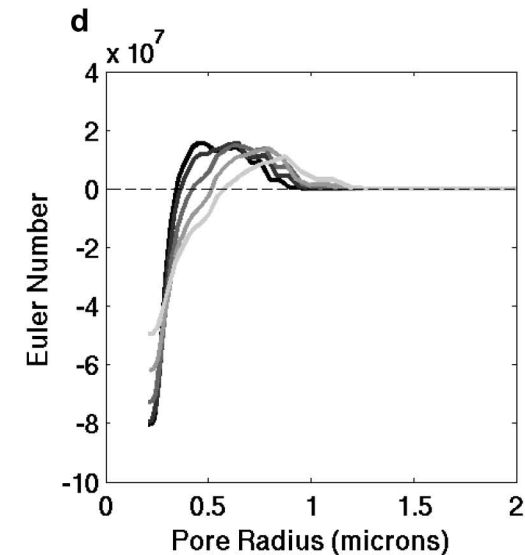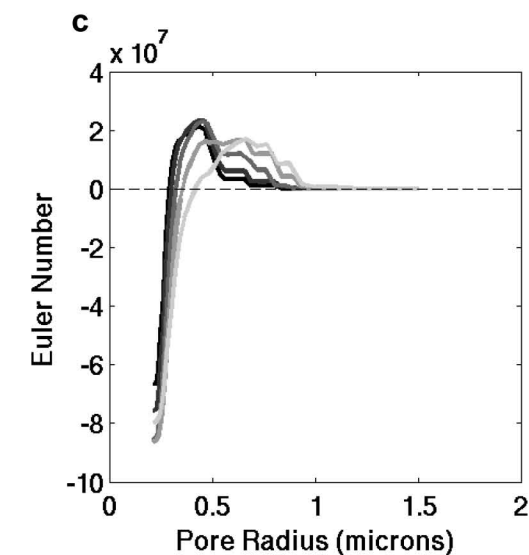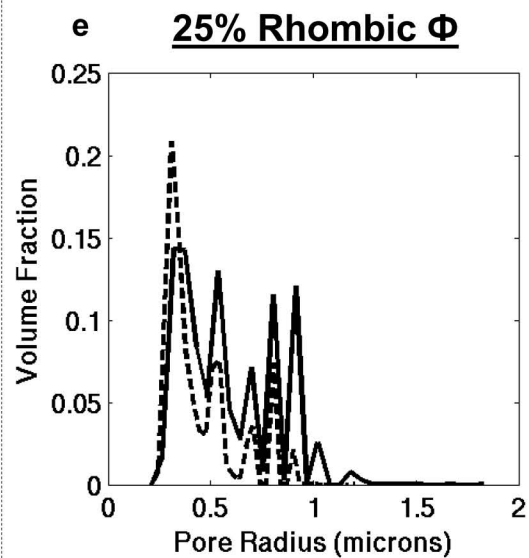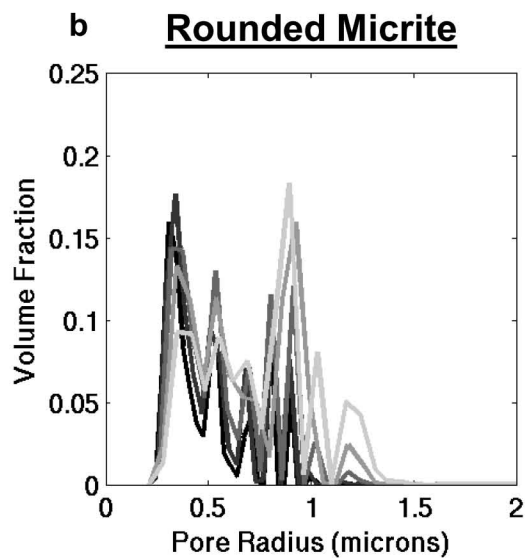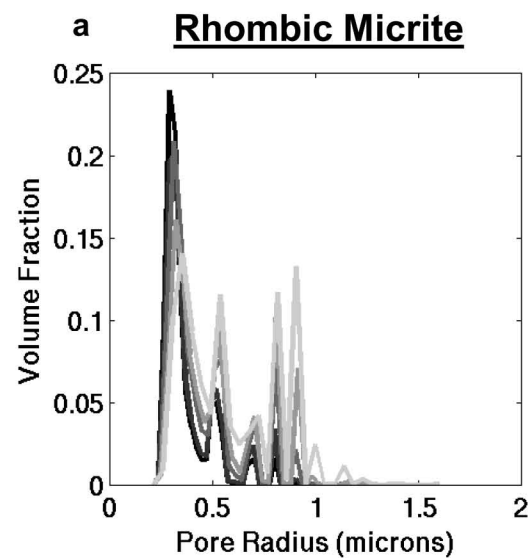
Legend:
—— 18%   —— 20%   —— 25%   —— 30%   —— 35%

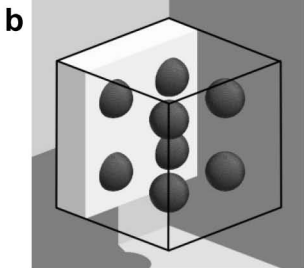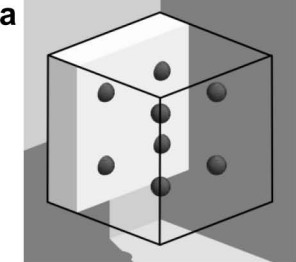- - - Rhombic Micrite
—— Rounded Micrite
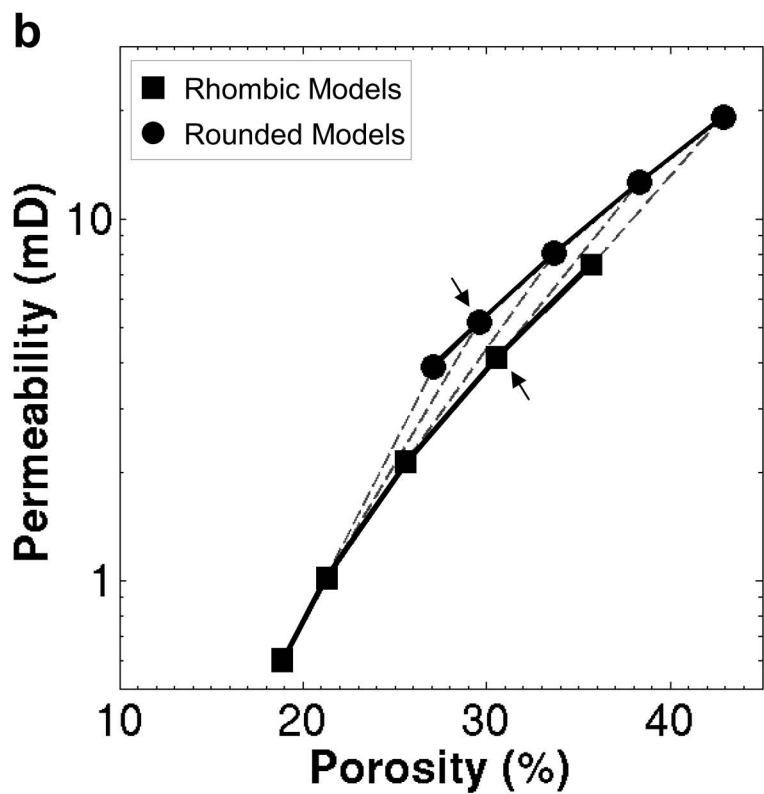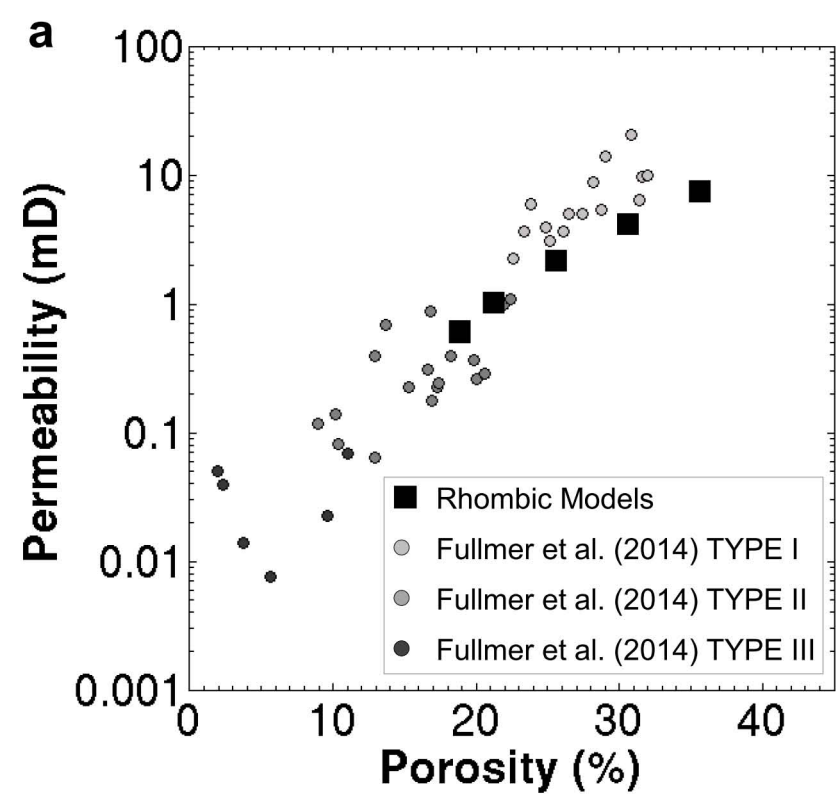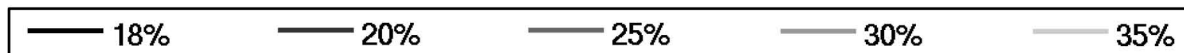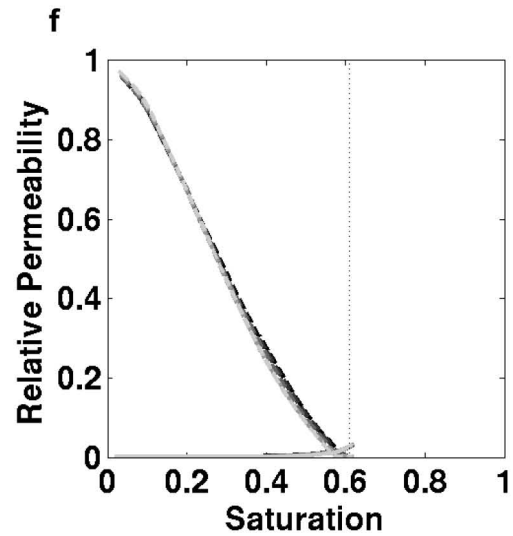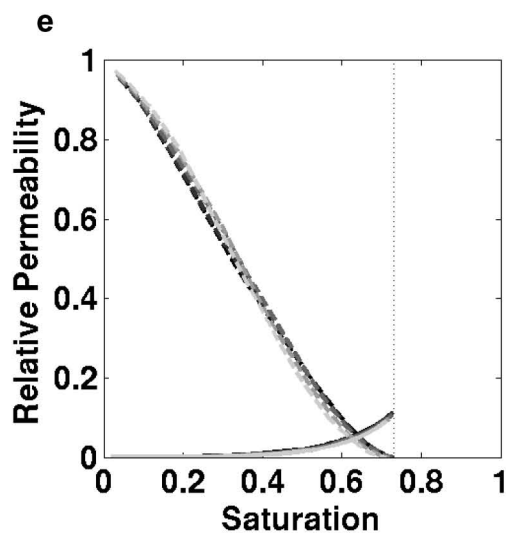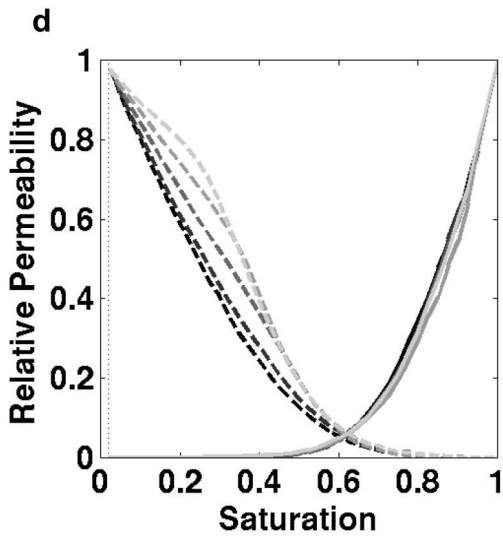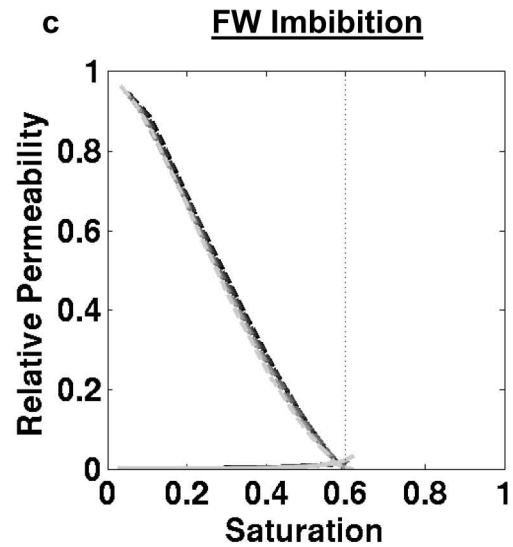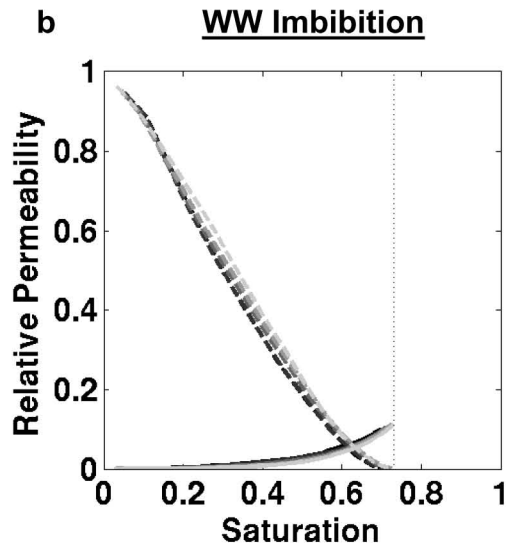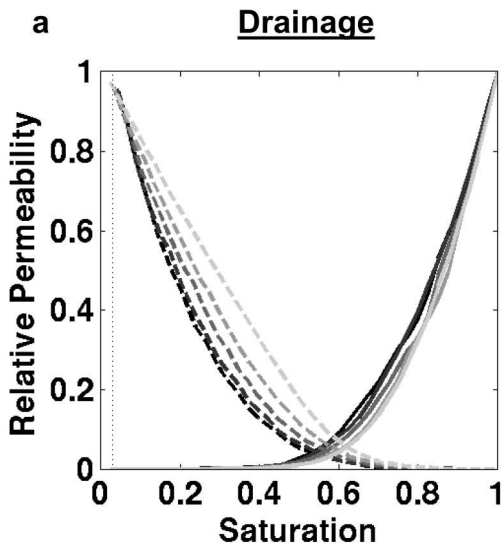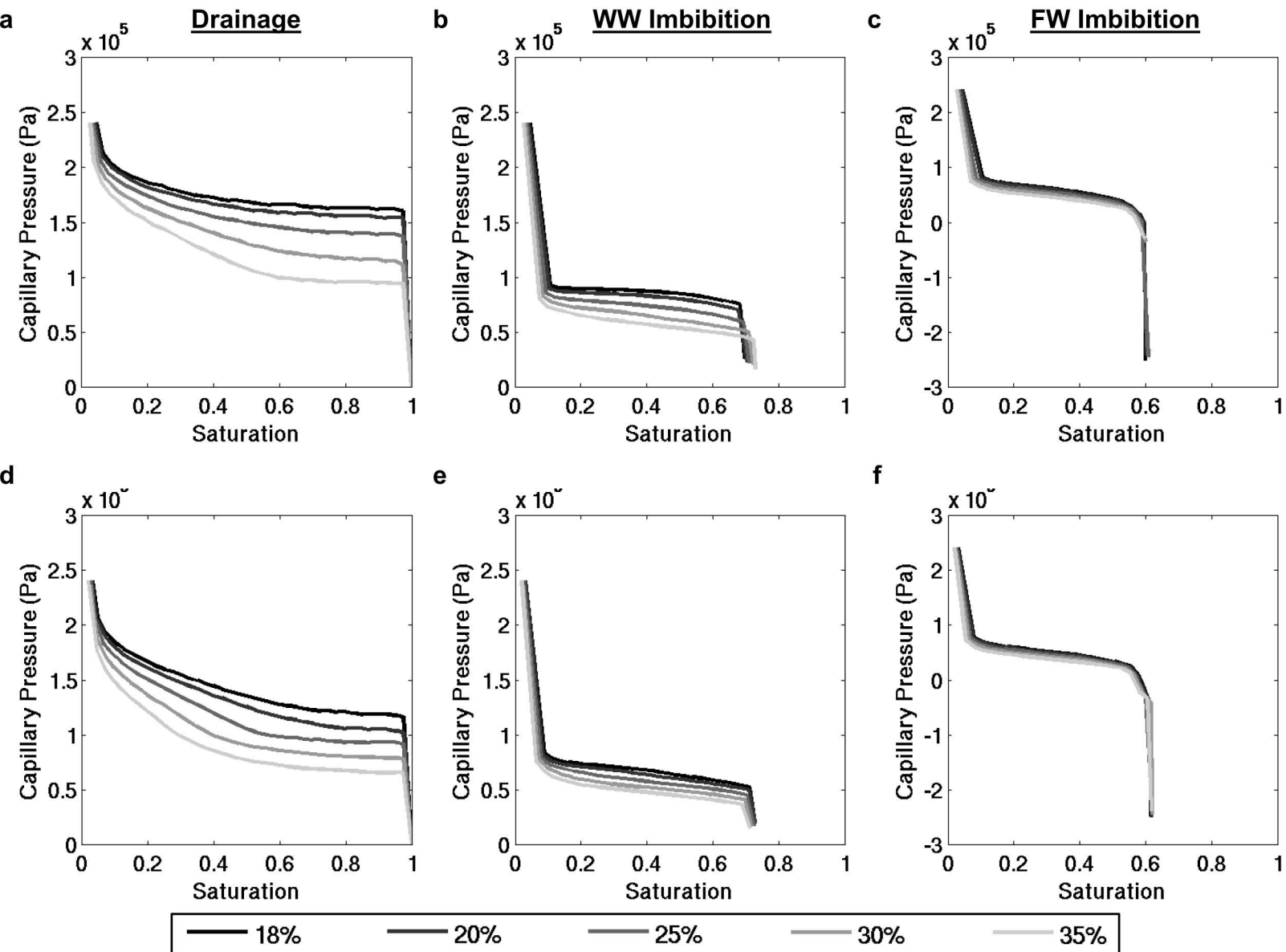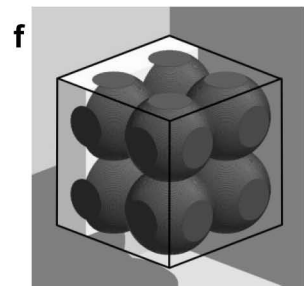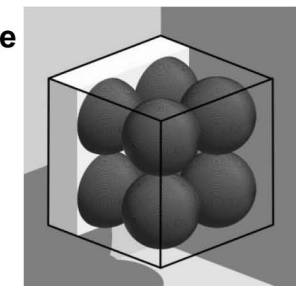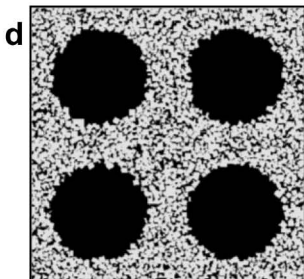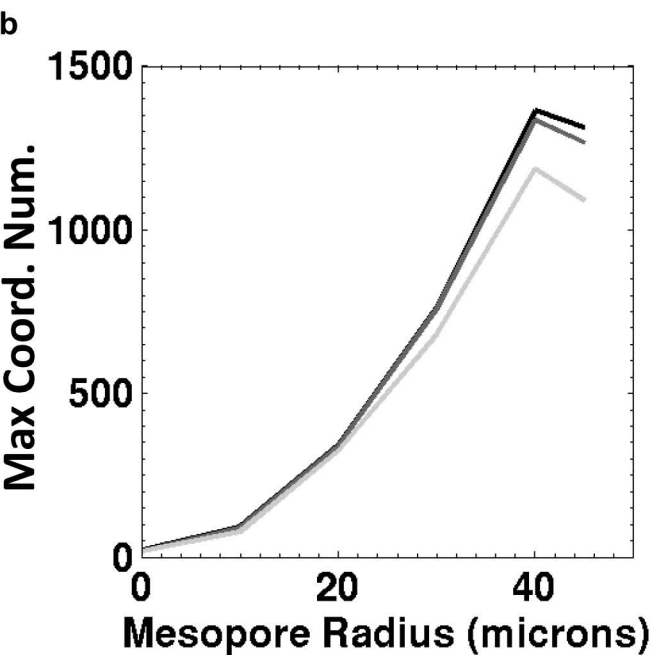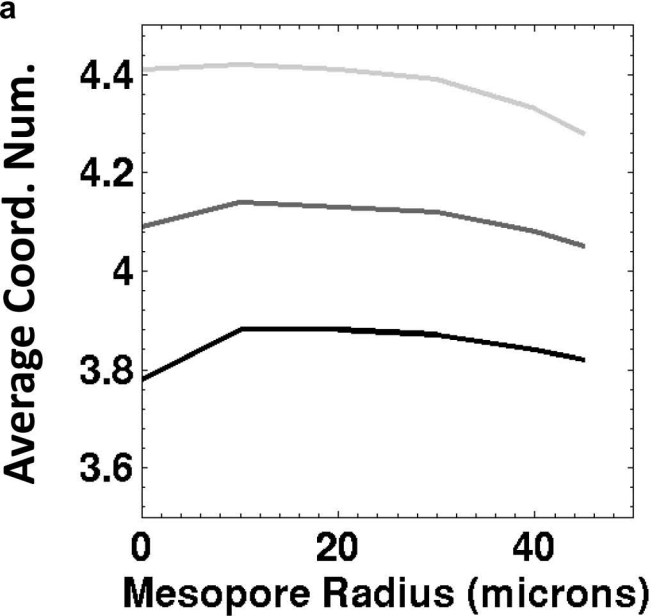
| a | Drainage | b | WW Imbibition | c | FW Imbibition |

Relative Permeability vs **Saturation**

| ——— 18% | ——— 20% | ——— 25% | ——— 30% | ——— 35% |
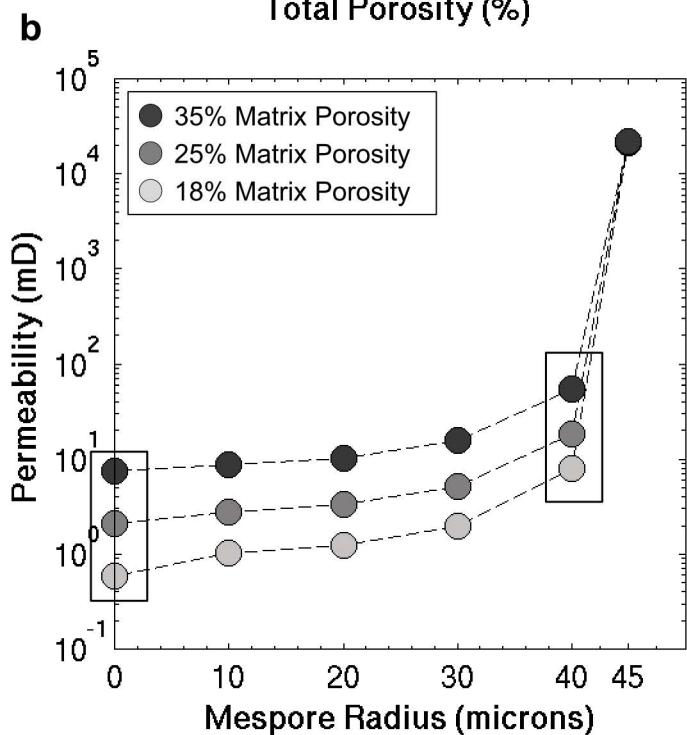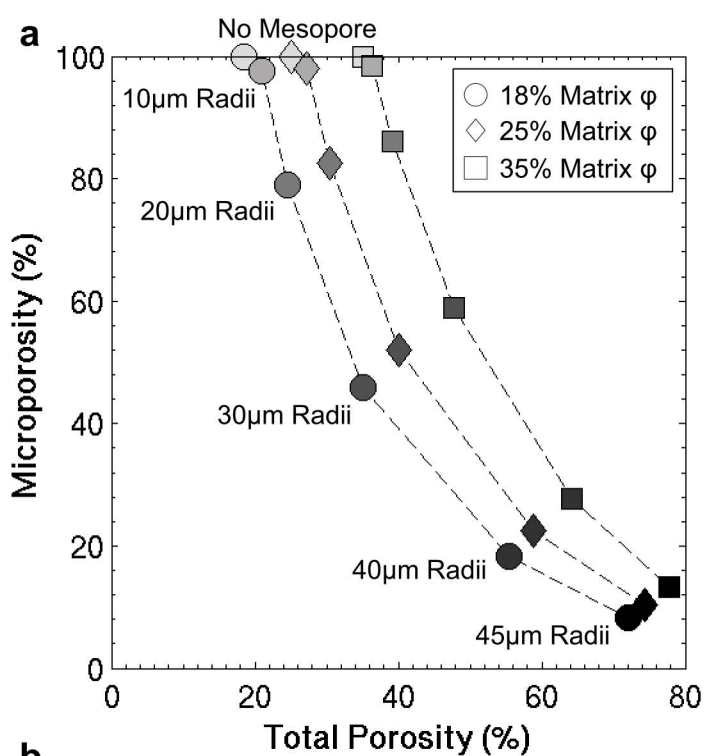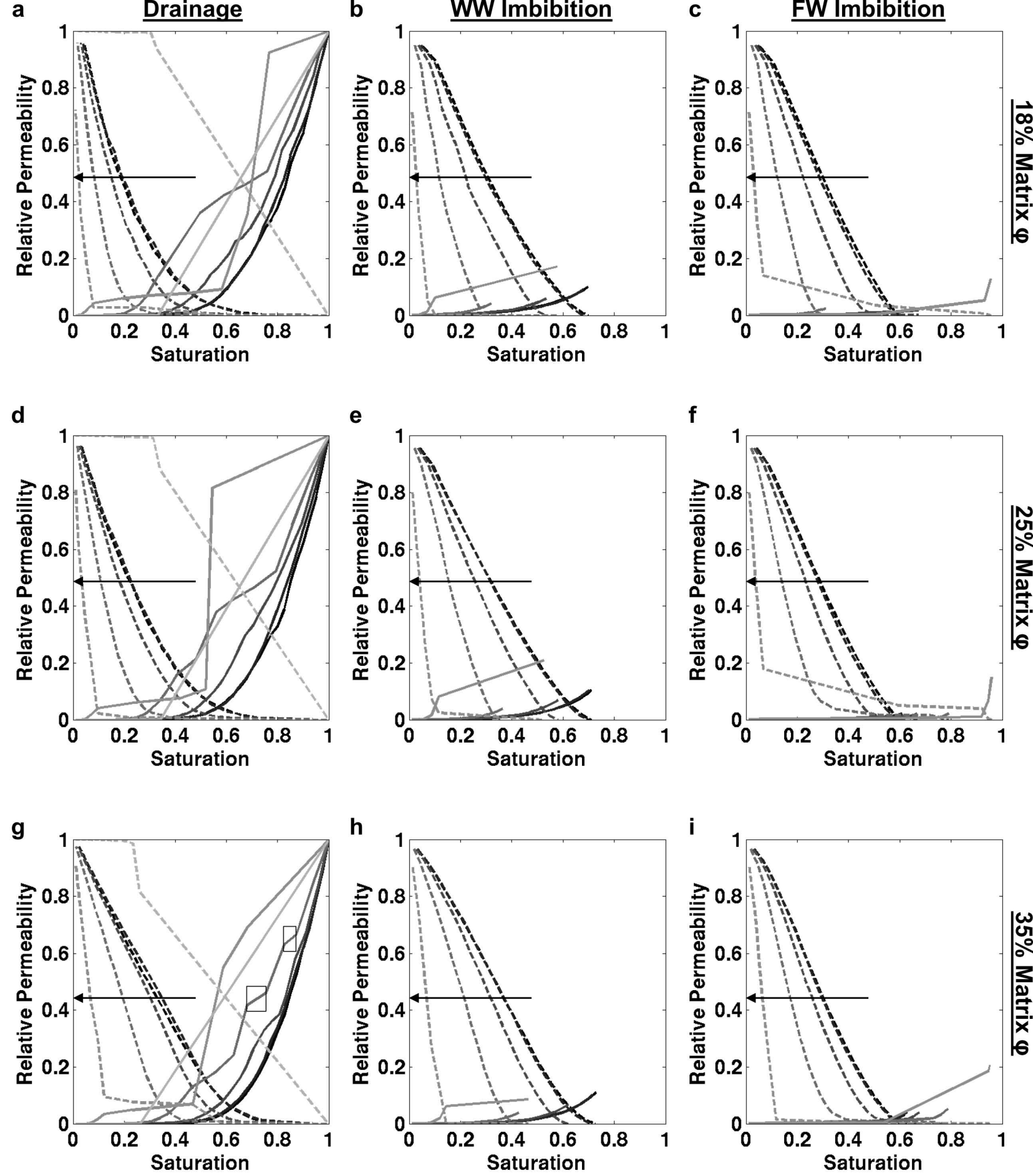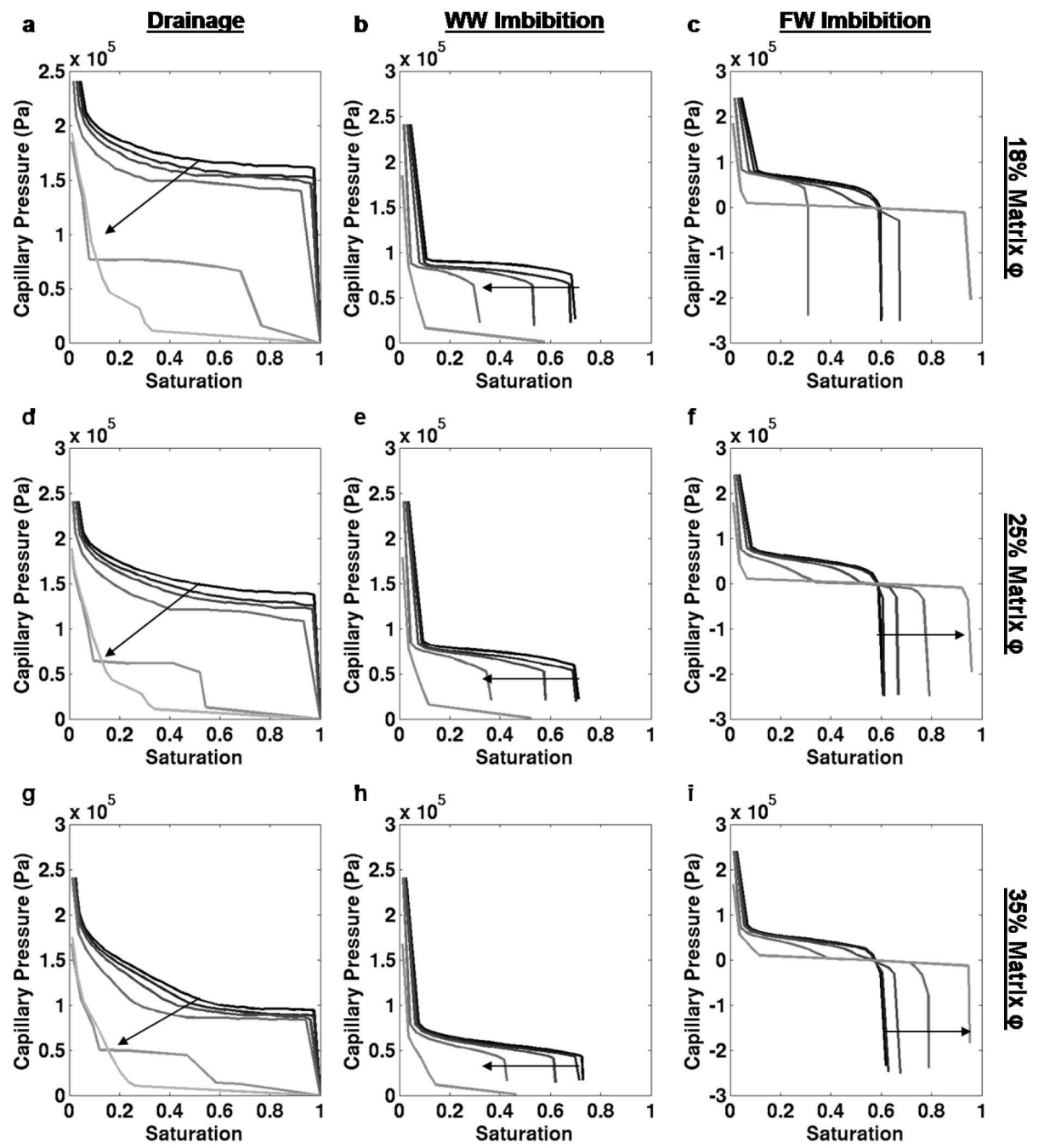
Drainage **WW Imbibition** **FW Imbibition**

a, b, c, d, e, f

Legend: 18% — 20% — 25% — 30% — 35%

a

b

—— 18% Matrix φ		—— 25% Matrix φ
—— 35% Matrix φ		

a

No Mesopore

10μm Radii

20μm Radii

30μm Radii

40μm Radii

45μm Radii

○ 18% Matrix φ
◇ 25% Matrix φ
□ 35% Matrix φ

Total Porosity (%)

Microporosity (%)

b

● 35% Matrix Porosity
● 25% Matrix Porosity
○ 18% Matrix Porosity

Permeability (mD)

Mespore Radius (microns)

a Drainage
b WW Imbibition
c FW Imbibition
18% Matrix φ

d Drainage
e WW Imbibition
f FW Imbibition
25% Matrix φ

g Drainage
h WW Imbibition
i FW Imbibition
35% Matrix φ

Relative Permeability vs. Saturation

■ No Mesopore   ■ 10μm Radius   ■ 20μm Radius   ■ 30μm Radius   ■ 40μm Radius   □ 45μm Radius

a Drainage   **b** WW Imbibition   **c** FW Imbibition

18% Matrix φ · 25% Matrix φ · 35% Matrix φ

No Mesopore · 10μm Radius · 20μm Radius · 30μm Radius · 40μm Radius · 45μm Radius

a   WW Imbibition

b   FW Imbibition